Azerbaijan Journal of Physics

FIZIKA

Ministry of Science and Education Republic of Azerbaijan
Institute of Physics

HONORARY EDITORS

Arif PASHAYEV

THE RADIAL DISTRIBUTION OF CURRENT DENSITY IN AN ELECTROHYDRODYNAMIC ION SOURCE BASED ON THE InSn ALLOY

Sh.O. EMINOV, S.A. ALIYEV, F.E. MAMMADOV, I.I. GURBANOV, E.M. AKBEROV, J.A. GULIYEV, A.A. BADALOV

Institute of Physics, Ministry of Science and Education of the Republic of Azerbaijan
AZ 1143, H. Javid Avenue 131, Baku, Azerbaijan
mammadov.f.e@gmail.com

The radial distribution of current density from the center of the beam to the edges across the radius of the emission field was investigated using a miniature probe target placed at a specific distance from the emission point at various beam current values from a liquid metal ion source with InSb as the working substance. It has been observed that despite the consistent geometric dimensions of the emission area at various emission current values, the current density decreases at measurement points from the center of the beam towards the edges. The experimental results provide the maximum opportunity to adjust the dimensions of thin layers deposited on various substrates using the ion source, as well as to ensure uniform thickness distribution across the surface of the samples.

INTRODUCTION

Presently, the deposition of thin layers of various elements and compounds onto surfaces is one of the most pertinent areas of research, and, of course, various methods known to science and technology are employed for this purpose. For example, magnetron sputtering, thermal evaporation, electron-beam evaporation, and others. Certainly electrohydrodynamic ion sources or ion sources from metal-liquid alloy (LMAIS) [1,2] are increasingly being used to obtain charged particles from various substances and alloys and deposit them onto different surfaces. The reason for this is that this method allows obtaining an intensive ion beam, requires a smaller amount of working substance for the ion source, allows for the control of the charged particle's exit velocity, the possibility of separating the particle beam based on their charge and mass, and so on. All of these provide additional capabilities to achieve the desired quality in the acquired delicate layers. However, the uneven distribution of current density in the emitted ion beam, which is highest at the center and decreases as you move away from the center, naturally leads to the formation of areas with varying thickness on the surface of the deposited layer, creating thin layers. Therefore, there is a need to study the radial distribution of current density in the beam [3,4]. Measuring the radial distribution of current in the beam provides the maximum opportunity to control the thickness of thin layers deposited on various substrates using ion sources. It helps in finding the optimal deposition mode when they are placed within the emission field. In this way, it is possible to achieve a uniform layer thickness across the entire surface of the samples.

InSb was used as the working material in the ion source. InSb is a widely studied semiconductor compound. The ease of synthesis and purification, as well as the high electron mobility at room temperature (which facilitates ionization), encourage the use of InSb. The energy bandgap of InSb at a temperature of 77 K is 0.27 eV, while at room temperature, it is 0.17 eV. The small bandgap of InSb allows it to be used as a photodetector in the near and mid-infrared range (3-5 μm). At the same time, this compound is used in the manufacturing of photodiodes, thermoelectric generators, as a Hall effect sensor, in devices that measure resistance changes in a magnetic field, and in various other applications. The deposition of ion compound layers based on InSb in an ion source allows for the creation of thin films and various surface structures, thereby expanding its range of applications.

EXPERIMENT

The experiment was conducted in a Leybold-Heraus A700Q vacuum system at a pressure of 5×10^{-6} mbar. The overall structural diagram of the ion source is presented in Figure 1 [5].

Initially, the needles, which are the primary components of the ion source, were manufactured using a special method from NiCr material and coated with InSb material in a vacuum environment. Afterward, the InSb-coated needle is placed inside a graphite container containing the working material and is installed in the ion source. To set up the experiment, a piezostage MC-2000 was placed inside the vacuum chamber, while the table control system was positioned outside the chamber. The connection is established between the table and the control panel, as well as between the control panel and the computer. All wiring and the table are shielded to prevent the impact of high voltage on the table control system. Additionally, a special collector with a diameter of 5 mm was prepared and installed on the piezostage to register the batch current (Figure 2). After taking all the necessary precautions, the experiment was conducted in a vacuum environment.
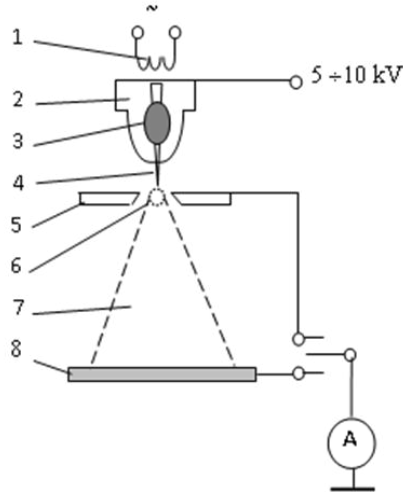
Fig. 1. Ion source diagram: 1 - cathode, 2 - container, 3 - working material, 4 - needle,
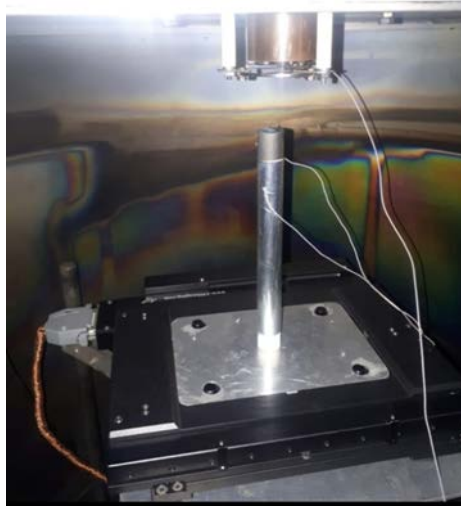5 - extractor, 6 - bright field, 7 - ion beam, 8 – collector

Fig. 2. Ion source in the vacuum chamber and the collector circuit located on the piezo stage.

The ion source was heated to the melting temperature of the working material using a tungsten cathode and then via thermionic emission. Subsequently, an accelerating voltage was applied between the extractor and the cathode, and ion emission occurred at a specific threshold voltage. When measuring the beam current in the collector circuit, the collector was displaced using the piezostage from the control panel located outside the chamber.

The most important characteristic of any ion column is the focusing of the ion beam to the smallest possible quasi-point dimensions [6]. The minimum diameter of the ion beam d at the target is determined by the formula

$$d = \sqrt{\left(Md_q\right)^2 + d_s^2 + d_c^2 + d_b^2} \qquad (1)$$

Where M is the optical magnification of the ion column, $d_q -$ is the virtual (imaginary) size of the source, $d_s -$ is the spot size due to spherical aberration, $d_c -$ the spot size due to chromatic aberration, and d_b is the diffraction spot.

Accordingly, d_q d_c and d_b are calculated using the following formulas:

$$d_s = \frac{1}{2}C_s\alpha^3, \quad d_c = C_c\left(\frac{\Delta E}{E}\right)\alpha, \quad d_b = 0{,}6\frac{\lambda}{\alpha}, \quad (2)$$

where $\alpha -$ is the angle of ion entry into the target, $C_s -$ is the coefficient of spherical aberration, $C_c -$ is the coefficient of chromatic aberration, $E -$ is the ion energy, $\Delta E -$ is its energy spread, and $\lambda -$ is the de Broglie wavelength of ions, which is calculated by the formula

$$\alpha^2 = \frac{I}{\pi M^2 \left(\frac{dI}{d\Omega}\right)} \qquad (3)$$

where $I -$ is the primary ion current, and $\Omega -$ is the angular spread of ions in the beam.

Analyzing equations (1) - (3), it can be concluded that the optical magnification of the ion column is initially determined by the size and design of the column, and its value can vary within small limits by adjusting the potential on the condenser lens. It's important to consider that the de Broglie

4

wavelength for ions is negligibly small compared to that of electrons, which is why the impact of diffraction on blurred spots is typically disregarded. The angle of ion entry (acceptance) is determined by the choice of the aperture limiting the ion current. At high ion currents (1-100 nA), spherical aberration makes the main contribution to the diameter of the ion beam, while in the range of moderate currents (10-50 pA), its influence becomes insignificant. At currents below 10 pA, the virtual size of the source becomes the primary contributor. Therefore, from a practical

standpoint, the beam diameter is significantly influenced by the accelerating voltage, the total ion current, the energy spread of ions, and the virtual size of the source. In the future, we will examine in more detail the relationship between these parameters and the type of ions used in EHD sources. As an example, Figure 3 shows the dependence of the gallium beam diameter on the ion current in comparison with the most well-known sources used in modern Focused Ion Beam (FIB) systems [7].
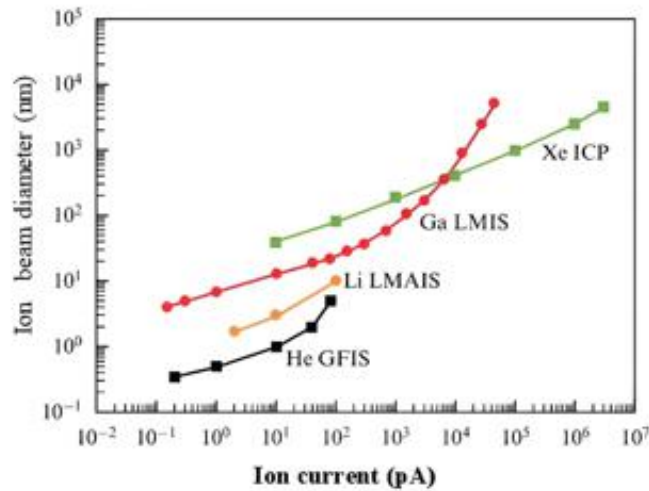
Fig. 3. The dependence of the ion beam diameter on the ion current for various sources used in modern Focused Ion Beam (FIB) systems [7].
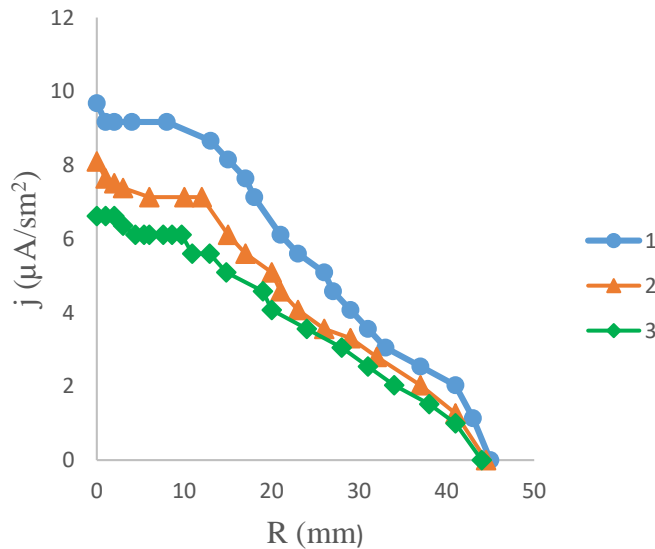
Fig. 4. Radial distribution of current density of the ion beam.
1) $I_{beam}=30\mu A$, U=6,3kV; 2) $I_{beam}=50\mu A$, U=6,5kV; 3) $I_{beam}=70\mu A$, U=6,5kV

The experiment was repeated at three different cluster current values (30 µA, 50 µA, 70 µA), and the radial distribution in the collector circuit was measured. The graphs of the radial current density distribution for each cluster current value are shown in Figure 4. When measuring the radial current

distribution, if the beam radius is known, it allows for the calculation of the total divergence angle of the ion beam. In our experiments, the distance between the collector and the ion source was approximately 42 mm, while the beam current radius was about 44 mm.

$$\alpha = 2 \ \text{arctg}\frac{l}{r} = 2 \ \text{cot}\frac{42}{44} = 2 \ \text{arctg}\,(1,04) \approx 2 \cdot 46° \approx 92°$$

Here, $l-$ represents the distance between the collector and the ion source, $r-$ is the radius of the current beam, and $\alpha-$ is the emission angle. In scientific literature, it has been demonstrated using transparent electron microscopes with electron energies of 1 MeV that the total scattering angle from the Taylor cone at the tip of the needle for materials such as Au, AuSi, CoGe, CoNd, In, Pb, and others during the ion emission process is in the range of 90° to 100° [8,9]. Clearly, the calculated emission angle in our experiments matches the values stated in the literature. This once again serves as strong evidence that we accurately determined the center of the ion beam during our measurements.

RESULTS

Measurements were conducted at three different cluster current values (30 µA, 50 µA, 70 µA). In all three cases, a point in the collector circuit where the cluster current had the maximum value was identified and taken as the center of the ion cluster. Then, the piezostage was set in motion, and the beam current magnitude was measured at intervals of approximately 1 mm. The current density value at each point was calculated based on the recorded beam current values. The calculated scattering angle, based on the dimensions of the ion source and the ion beam from the emitter, corresponds to the sizes obtained by other authors and accepted in the literature.

[1] *Lothar Bischoff, Paul Mazarov, Lars Bruchhaus, and Jacques Gierak.* Liquid metal alloy ion sources—An alternative for focussed ion beam technology. Applied Physics Reviews 3, 021101 (2016); https://doi.org/10.1063/1.4947095

[2] *Mazarov P., Dudnikov V.G., Tolstoguzov A.B.* Electrohydrodynamic emitters of ion beams. Phys. Usp. 63 1219–1255 (2020); https://doi.org/10.3367/UFNr.2020.09.038845

[3] *I.S. Gasanov, I.I. Gurbanov.* About the sizes of emitters of ions and nanoparticles in point sources. Applied physics №. 1, 2010, p. 55-57.

[4] *I.S Gasanov, I.I. Gurbanov.* Nanostructure operations by means of the liquid metal ion sources. Review of scientific instruments 83, 02 B 906 (2012) https://doi.org/10.1063/1.3670340

[5] *I.S. Gasanov, I.I. Gurbanov.* Formation of Charged Nanodroplets at Capillary Instability of the Liquid Emitter. Japanese Journal of Applied Physics Vol. 47, №. 10, 2008, pp. 8226–8229 https://doi.org: 10.1143/JJAP.47.8226

[6] *P.D. Prewett, G.L.R. Mair.* Fokused Ion Beams from Liquid Metal Ion Source. Research Studies Press, 1991 https://doi.org/10.1016/0042-207X(92)90309-K

[7] *Klinqner N. et al.* Imaging and milling resolution of light ion beams from helium ion microscopy and FIBs driven by liquid metal alloy ion sources. Beilstein J. Nanotechnol. 2020, 11, 1742–1749. https://doi.org/10.3762/bjnano.11.156

[8] *W. Driesel, C. Dietzsch.* In situ HVTEM observation of the tip shape of tin liquid metal ion sources. Applied Surface Science, Vol 93, Issue 2, 1 February 1996, p.179-190, https://doi.org/10.1016/0169-4332(95)00326-6

[9] *Chase S. Coffman, Manuel Martínez-Sánchez, and Paulo C. Lozano.* Electrohydrodynamics of an ionic liquid meniscus during evaporation of ions in a regime of high electric field. Phys. Rev. E 99, 063108, 26 June 2019 https://doi.org/10.1103/PhysRevE.99.063108

HEAT CAPACITY OF ELECTRONS IN KANE-TYPE SEMICONDUCTOR TUBE

A. M. BABANLI

Department of Physics, Süleyman Demirel University, 32260 Isparta, Turkey
arifbabanli@sdu.edu.tr

The energy spectrum and heat capacity of Kane electrons on the surface of a nanotube are investigated. It is shown that for high temperatures the specific heat of Kane electrons on the surface of a nanotube is 4 times greater than the specific heat of the semiconductor nanotube with parabolic dispersion laws and for low temperatures the specific capacity is equal to $2k_B$.

Recently, low-dimensional semiconductor systems have become the object of great interest due to their wide application in technology. Scientists are increasingly interested in semiconductor heterostructures with curved surfaces, quantum dots, and nanotubes.

The extraordinary electrical properties of nanotubes make them one of the main materials of nanoelectronics [1,2]. Nanometer-sized electronic devices are created based on nanotubes. Thermodynamic properties of the electron gas on the surface of a nanotube have been studied in Ref. [3]. An analytical expression for the energy of a relativistic electron on a nanotube in an external magnetic field was obtained using the Dirac equation in [4].

In the work [4], authors utilized the Dirac equation to find the energy of electrons on the nanotube surface in the presence of a magnetic field. Using this energy spectrum, the thermodynamic functions of the nanotube at low and high temperatures were calculated. Rubens R.S. et al [5] calculated the thermodynamic properties of the quantum ring according to the solutions of both Dirac and Schrödinger equations. Ref. [6] Ermolaev studied the thermodynamic properties of degenerate and non-degenerate electron gas on the semiconductor nanotube surface in a magnetic field.

The heat capacity and magnetic properties of electrons in superlattices on the surface of the nanotube in a magnetic field orientated along the axis of the nanotube were studied in [7]. In paper [8], the energy spectrum of the one-dimensional Kane oscillator was found, and it was found that the heat capacity is four times larger than the heat capacity of the one-dimensional harmonic oscillator at high temperatures.

Ref. [9] studied the heat capacity and magnetic moment of a lattice of non-interacting nanotubes in a magnetic field.

In this paper, the standard tube model is used: a sheet of non-interacting 2D electron gas is twisted into a tube shape. This model allows us to obtain the energy spectrum of electrons on the nanotube surface. In this study, we used the Kane model, which takes into account the interaction of the conduction and the valence bands. Kane's model allows us to express the energy spectra of electrons, light holes, and spin-orbital splitting holes on the surface of the nanotube. Using the energy spectrum of carriers on the surface of a tube calculated the heat capacity of non-degenerate electrons in a Kane-type semiconductor tube. The study of the heat capacity of objects is very important in physics since the specific heat depends on the internal state of the substance and the movement of its constituent particles.

We consider a non-interacting two-dimensional electron gas on the nanotube surface out of Kane type semiconductor. The Kane equations has the form [10]:

$$-EC_1 - \frac{Pk_-}{\sqrt{2}}C_3 + \sqrt{\frac{2}{3}}Pk_z C_4 + \frac{Pk_+}{\sqrt{6}}C_5 + \sqrt{\frac{1}{3}}Pk_z C_7 + \frac{Pk_+}{\sqrt{3}}C_8 = 0 \tag{1}$$

$$-EC_2 - \frac{Pk_-}{\sqrt{6}}C_4 + \sqrt{\frac{2}{3}}Pk_z C_5 + \frac{Pk_+}{\sqrt{2}}C_6 + \frac{Pk_-}{\sqrt{3}}C_7 - \sqrt{\frac{1}{3}}Pk_z C_8 = 0 \tag{2}$$

$$-\frac{Pk_+}{\sqrt{2}}C_1 - \left(E + E_g\right)C_3 = 0 \tag{3}$$

$$\sqrt{\frac{2}{3}}Pk_z C_1 - \frac{Pk_+}{\sqrt{2}}C_2 - \left(E + E_g\right)C_4 = 0 \tag{4}$$

$$\sqrt{\frac{2}{3}}Pk_zC_2 + \frac{Pk_-}{\sqrt{2}}C_1 - \left(E + E_g\right)C_5 = 0 \tag{5}$$

$$\frac{Pk_-}{\sqrt{2}}C_2 - \left(E + E_g\right)C_6 = 0 \tag{6}$$

$$\frac{Pk_+}{\sqrt{3}}C_2 + \sqrt{\frac{1}{3}}Pk_zC_1 - \left(E + E_g + \Delta\right)C_7 = 0 \tag{7}$$

$$\frac{Pk_-}{\sqrt{3}}C_1 - \sqrt{\frac{1}{3}}Pk_zC_2 - \left(E + E_g + \Delta\right)C_8 = 0 \tag{8}$$

The parameter P characterizes the interaction between the conduction and valence bands. E_g the band gap energy, $\varDelta$ the value of spin–orbital splitting, and $k_{\pm} = k_x \pm ik_y$ $\vec{k} = i\vec{\nabla}$, C_i are envelope functions. Substituting expressions (3)–(8) into formulas (1) and (2) we obtain

$$\left\{ -E - \frac{P^2}{3}\left[\frac{2}{E + E_g} + \frac{1}{E + E_g + \Delta}\right]\Delta_3 \right\}C_{1,2} = 0 \tag{9}$$

where $\varDelta_3$ is the three-dimensional Laplacian. In cylindrical coordinates the eigenfunctions

$$C_{1,2} = A\exp\left(im\varphi + ik_z z\right)Q_{1,2} \tag{10}$$

where A is a normalization factor and the energy spectrum of carriers in a Kane-type semiconductor tube is satisfies

$$\left(\frac{3}{P^2}\frac{E(E + E_g)(E + E_g + \Delta)}{(3E + 3E_g + 2\Delta)} - \left(\frac{m^2}{\rho^2} + k_z^2\right)\right)^2 = 0 \tag{11}$$

As can be seen from the formula (11), the energy spectra of charge carriers are doubly degenerate. For the strong spin-orbit approximation $\Delta \to \infty$ Eq. (11) transforms as

$$E(E + E_g) = \frac{2P^2}{3}\left(\frac{m^2}{\rho^2} + k_z^2\right) \tag{12}$$

The matrix element P^2 is expressed in terms of the effective mass of electrons m_n as

$$\frac{2P^2}{3E_g} = \frac{\hbar^2}{2m_n} \tag{13}$$

If we choose zero of energy in the middle of the energy gap $E \to E - \frac{E_g}{2}$ we find

the energy levels of electrons (sign +) and light holes

$$E = \pm\sqrt{\frac{E_g^2}{4} + \frac{\hbar^2 E_g}{2m_n}\left(\frac{m^2}{\rho^2} + k_z^2\right)} \tag{14}$$

The expression inside the square root is the sum of the square of the energy of the motion of the electron along the axis of the tube and the square of the energy of the charged rotator in the magnetic field. The canonical partition function is defined as

$$z = \sum_{mk_z} e^{-\beta E_{mk_z}} \tag{15}$$

$\beta = (k_B T)^{-1}$, k_B —is the Boltzmann constant. The summation over k_z can be transformed into integral as:

$$z = \sum_{mk_z} e^{-\beta E_{m\sigma k_z}} = \frac{L}{2\pi} \sum_m \int_0^\infty dk_z e^{-\beta \sqrt{\frac{\hbar^2 E_g}{2m_n} k_z^2 + u_m^2}} \tag{16}$$

where

$$u_m = \sqrt{\frac{E_g^2}{4} + \frac{\hbar^2 E_g}{2m_n \rho^2}} \tag{17}$$

The integral over k_z can be calculated by substituting

$$k_z = \left(\frac{\hbar^2 E_g}{2m_n}\right)^{-\frac{1}{2}} u_{m\sigma} sh\theta \tag{18}$$

By using the following formula [11]

$$K_\nu(x) = \int_0^\infty d\theta \, ch(\nu\theta) e^{-xch\theta} \tag{19}$$

we find the partition function as

$$z = \frac{L}{\pi} \left(\frac{\hbar^2 E_g}{2m_n}\right)^{-\frac{1}{2}} \sum_m u_m K_1(\beta u_m) \tag{20}$$

If we ignore the quantization of the circular motion and go from summation to integration for the quantum number m, we get

$$\sum_{m=-\infty}^\infty \to \int_{-\infty}^\infty dt \tag{21}$$

where

$$t = \sqrt{\left(u^2 - \frac{E_g^2}{4}\right)\left(\frac{\hbar^2 E_g}{2m_n \rho^2}\right)^{-1}} \tag{22}$$

We use the following formula [12]

$$\int_a^\infty x^{1\pm\nu} \left(x^2 - a^2\right)^{\beta-1} K_\nu(cx) dx = 2^{\beta-1} c^{-\beta} \Gamma(\beta) K_{\nu\pm\beta}(ac) \tag{23}$$

We have the partition function as

$$= \frac{L}{\pi\rho} \left(\frac{\hbar^2}{2m_n \rho^2}\right)^{-1} 2^{\overline{2}} \left(\frac{g}{2}\right)^{\frac{1}{2}} \Gamma\left(\frac{1}{2}\right) \beta^{-\frac{1}{2}} K_{3/2}\left(\beta \frac{E_g}{2}\right) \tag{24}$$

The heat capacity is defined as

$$C = k_B \beta^2 \frac{\partial^2}{\partial \beta^2} \ln z \tag{25}$$

If $\beta \frac{E_g}{2} \ll 1$, we should use [11]

$$K_\nu(x) \approx \frac{1}{2} (\nu)\left(\frac{x}{2}\right)^{-\nu} \tag{26}$$

From (25) we find $C = 2k_B$ at $T \to \infty$. Since the energy spectrum of the Kane electrons is 2-fold degenerate, the specific heat of Kane electrons is 4 times greater than the specific heat of the semiconductor nanotube with parabolic dispersion

laws [9]. If $\beta \dfrac{E_g}{2} >> 1$ we can use the asymptotic formula

$$K_\nu(x) \approx \sqrt{\frac{\pi}{2x}} e^{-x} \left(1 + \frac{4\nu^2 - 1}{8x}\right) \qquad (27)$$

The heat capacity is now reduced $C = k_B$. Unlike tubes with a parabolic dispersion law, the specific heat of electrons in Kane tubes is $2\ k_B$ at low temperatures.

CONCLUSIONS

In this work, the energy spectrum and heat capacities of electrons on the surface of Kane-type semiconductor tubes are calculated, taking into account the nonparabolicity energy spectrum of electrons. it is shown that the heat capacity is equal to 4 kB at high temperatures and 2 kB at low temperatures.

_____

[1] *R. Saito, G. Dresselhaus, M.S. Dresselhaus.* Physical Properties of Carbon Nanotubes, Imperial College Press, London, 1998.

[2] *P.N. Dyachkov.* Electronic Properties and Application of Nanotubes, Binom. Laboratory of Knowledge, Moscow, 2012.

[3] *A.M. Ermolaev and G.I. Rashba.* J. Phys. Condens. Matter 20, 175212 (2008)

[4] *N.V. Gleizer, A.M. Ermolaev and G.I. Rashba.* International Journal of Modern Physics B Vol. 33, №. 22 (2019) 1950253

[5] *Rubens R.S. Oliveira, Adailton A. Araʹujo Filhob, Francisco C.E. Limac, Roberto V. Malufd, and Carlos A.S. Almeida.* Eur. Phys. J. Plus (2019) 134: 495

[6] *A.M. Ermolaev and G.I. Rashba.* Eur. Phys. J. B 73, 383–388 (2010)

[7] *A.M. Babanlı.* Low Temperature Physics/Fizyka Nyzkykh Temperatur, 2023, Vol. 49, №. 2, pp. 220–224

[8] *A.M. Babanlı.* Fizyka Nyzkykh Temperatur/Low Temperature Physics, 2023, Vol. 49, №. 10, pp.

[9] *A.M. Babanlı.* Journal of Magnetism and Magnetic Materials, 15,2022, 169876

[10] *F.M. Gashimzade, A.M. Babayev, S. Çakmak, Ş. Çakmaktepe.* Physica- E 23, Issues 1–2, June 2004, Pages 177-182

[11] *M. Abramowitz and I. A. Stegun.* Handbook of Mathematical Functions (National Bureau of Standards, Washington, 1964)

[12] *В.А. Диткин, А.П. Прудников.* Интегральные преобразования и операционное исчисление. М.: ГИФМЛ, 1961.

Received: 28.09.2023

PREPARATION AND PROPERTIES OF PHOTOSENSITIVE
$Cu_3In_5S_9$ THIN FILMS

A.I. BAYRAMOVA[1], A.G. GUSEINOV[2]

[1]Azerbaijan University of Architecture and Construction
[2]Baku State University
*aynurabayramova09@gmail.com*

Highly photosensitive thin films of the $Cu_3In_5S_9$ compound were obtained by the method of instantaneous thermal evaporation of a substance in vacuum. Impurity photoconductivity and an impurity absorption band with a maximum at 1,15 eV were detected. It is assumed that the high concentration of impurity electronic states is due to the presence in the films of a high concentration of cation and anion vacancies in the structure of the crystal lattice.

INTRODUCTION

The scientific literature provides data on the existence in the Cu-In-S ternary system of ternary semiconductor phases $CuInS_2$, $CuIn_{11}S_{17}$, $CuIn_5S_8$, $Cu_3In_2S_6$ and $Cu_3In_5S_9$, which have relatively close melting temperatures and a narrow region of homogeneity in the phase diagram [1]. Studies of the physical properties of these phases have shown their features that are of practical interest in the fields of photonics, optics, optoelectronics and photocatalysis [2-6]. The production of Cu-In-S thin films by spray pyrolysis [7] showed that the composition of the deposited thin film predominantly corresponds to the chemical formula $Cu_3In_5S_9$. The semiconductor compound $Cu_3In_5S_9$ is formed in a quasi-binary system according to the reaction formula

$$3Cu_2S + 5In_2S_3 \rightarrow 2\ Cu_3In_5S_9$$
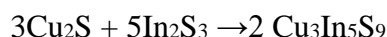
Crystals of the In_2S_3 compound are defective crystals and, depending on temperature, have α-, β- and γ-phase states. The crystal structure refers to a spinel structure in which cation vacancies are randomly arranged in octahedral or octahedral and tetrahedral positions. The $CuIn_5S_8$ compound also crystallizes in a spinel structure and has 25% vacancy in the cation sublattice and is classified as a defect crystal.

It was shown in [8] that the compound $Cu_3In_5Te_9$, isostructural to $Cu_3In_5S_9$, also has 11.6% vacancies in the cation sublattice of the crystal structure. The $Cu_3In_5S_9$ compound crystallizes in a monoclinic structure with cell parameters a = 0,660 nm, b = 0,691 nm and c = 0,812 nm and β = 890 [8]. $Cu_3In_5S_9$ single crystals are brittle and easily break off mechanically along the crystallographic c axis, forming a mirror-smooth surface.

PREPARATION AND EXPERIMENTAL PROCEDURE

The $Cu_3In_5S_9$ compound was synthesized in an evacuated quartz ampoule with a conical end, by direct melting of individual components taken in stoichiometric ratios. The synthesis of a charge with a total weight of 20 g was carried out in a horizontal position of the ampoule. Therefore, the substance was evenly distributed along the length of the ampoule and had a homogeneous large-block composition. Thin films of $Cu_3In_5S_9$ were obtained by thermal evaporation of a grain of crystal dust in a vacuum chamber. The synthesized substance was crushed into dust particles with an average size of 100 mkm and poured into a hopper equipped with a special device capable of controlled delivery of the substance into a glass ceramic crucible. After filling, the chamber was pumped out to 10^{-5} mm Hg. Art. and the crucible was heated to 1240°C. Dust particles entering the crucible instantly evaporated without contacting the walls of the crucible. High-quality glass-ceramic was used as a substrate.

The photoconductivity of thin films was measured in a stationary mode by irradiating the sample with light from a halogen lamp. A diffraction monochromator with double dispersion was used as a monochromator. Photoluminescence of thin films was studied under the influence of second harmonic radiation (532 nm) of a pulsed Nd:YAG laser. The duration and power of the light pulse were 12 ns and 0,4 MW, respectively.

EXPERIMENTAL RESULTS AND DISCUSSIONS

Thin films of $Cu_3In_5S_9$ obtained by the above method had high photosensitivity. The ratio of the dark resistance of the film to the resistance illuminated with white light of 200 Lux of a sample with a thickness of 0,5 mm was $\geq 10^2$ times.

In Figure 1 shows the photocurrent spectra of a $Cu_3In_5S_9$ thin film at temperatures of 100 K (1) and 300K (2), calculated per unit photon. Photocurrent

spectrums cover a fairly wide range of radiation energies (0,9...3,3 eV). Taking into account the data from [8], the long-wavelength edge of the spectrum in the range of 0,9...1,5 eV is formed by impurity photoconductivity, since the band gap of the $Cu_3In_5S_9$ crystal is 1,62 eV at 15 K. The maximum photosensitivity of thin films is achieved at about 2 eV

photon energy. With an increase in temperature from 100 K to 300 K, the maximum of the spectrum increases almost 3 times. Considering that the spectra of a thin film covers a significant part of the solar radiation spectrum on the Earth's surface, we can recommend $Cu_3In_5S_9$ films as the active substance of a solar cell.

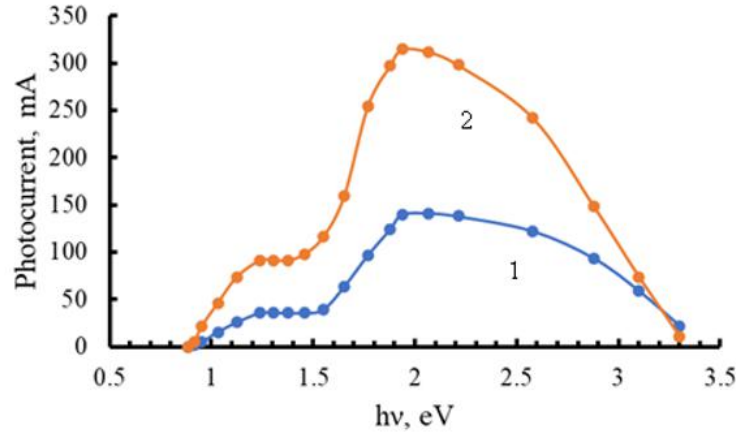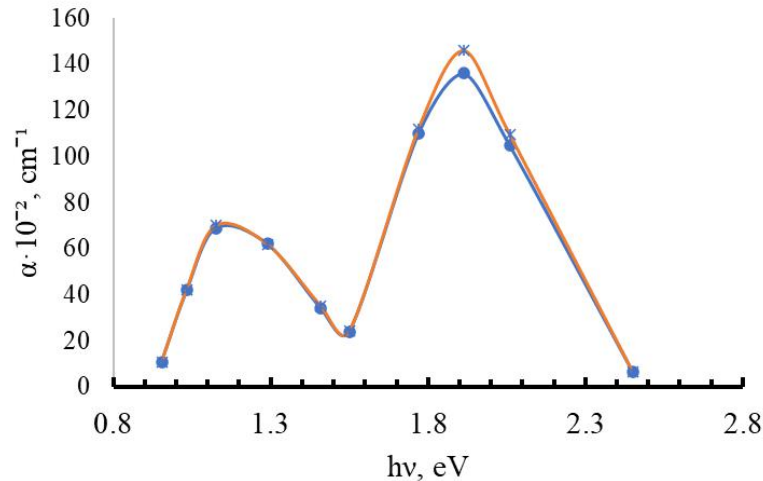*Fig. 1.* Photocurrent spectra of a $Cu_3In_5S_9$ thin film at temperatures of 100 K (1) and 300 K (2).

Fig. 2. $Cu_3In_5S_9$ spectra of the absorption coefficient of the thin layer.

The absorption coefficient spectra of $Cu_3In_5S_9$ thin films are in agreement with the photocurrent spectrum (Fig. 2). Impurity absorption in the absorption coefficient spectrum of a thin film is expressed as an absorption band with a maximum of 1,15 eV. The value of the impurity absorption maximum is approximately two times lower than the intrinsic absorption maximum. This means that in a thin film of $Cu_3In_5S_9$ there is a huge concentration of impurity states caused by cation and anion vacancies of the crystal lattice.

As a result of various studies, donor levels with burial depths $E_{D1}=0,017eV$, $E_{D2} = 0,28eV$, $E_{D3} = 0,76eV$

and an acceptor level with activation energy $E_A=0,16eV$ were identified in $Cu_3In_5S_9$ crystals. Therefore energy

$$\Delta E = E_g - (E_{D2} + E_A) = 1,18\ eV \tag{1}$$

It turns out that it is close to the maximum of impurity absorption and therefore it can be assumed that in the crystal there is a large concentration of donor and acceptor impurity states, which determine the impurity absorption.

The impurity absorption coefficient is expressed by the formula [10]:

$$K = \frac{256\pi e^2\ \hbar |P_{vc}|^2 E_v^{\frac{1}{2}}}{Rcm^2\hbar\omega(m_c E_D)^{3/2}} \sum_v \frac{m_p^{\frac{3}{2}}}{[1+(m_v E_v/m_c E_D)]} (N_D - n_D) \tag{2}$$

where, (N$_D$-n$_D$) is the concentration of free electronic states at donor levels, R is the reflection index, P$_{vc}$ is the matrix element of the momentum operator, E$_v$=ℏω-E$_D$-E$_g$ is the kinetic energy of the electron in the valence band. As can be seen in (2), the absorption coefficient linearly depends on the concentration of free electronic states at donor levels. The comparable values of the impurity and intrinsic absorption coefficients indicate the presence of a high concentration of donor and acceptor electronic states, caused by cationic and anionic vacancies of the crystal lattice.
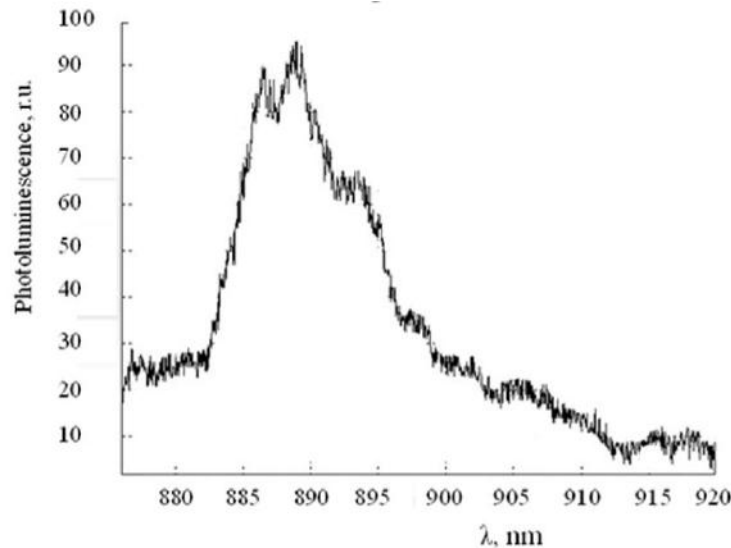

Fig. 3. Photoluminescence spectrum of a Cu$_3$In$_5$S$_9$ thin film excited by a laser pulse.

The photoluminescence spectrum of a Cu$_3$In$_5$S$_9$ thin film at 300 K is shown in Fig. 3. The spectrum covers the region of impurity absorption, and the maximum emission is observed at 1,39 eV. Apparently, in the recombination of nonequilibrium electrons excited by laser radiation, the main role will be played by the depleted donor level with a depth of E_{D2}=0,28eV.

[1] *Vasyl Tomashik.* Cu–In–S (Copper- Indium-Sulfur). Non-Ferrous Metal Systems. Springer-Verlag Berlin, Heidelberg, 2006; V11C1(1): p. 300-318

[2] *Alice D. P. Leach, Janet E. Macdonald.* J. Phys. Chem. Lett. 2016, 7, 3, pp. 572–583

[3] *Shigeru Ikeda, Takayuki Nakamura, Sun Min Lee, Tetsuro Yagi, Takashi Harada, Tsutomu Minegishi, Michio Matsumura.* Chemistry-Europe, ChemSusChem, 2011, Volume 4, Issue 2, pp. 262-268.

[4] *Shuming Liu, Lijuan Chen, Tingting Liu, Sheng Cai, Xiaoxiao Zou, Jingwen Jiang, Zhiyuan Mei, Zhihui Gao, Hong Guo.* Chemical Engineering Journal, Volume 424, 2021, p. 130325.

[5] *Gary Hodes, Tina Engelhard, John A. Turner, David Cahen.* Solar Energy Materials, (1985), Volume 12, Issue 3, Pages 211-219.

[6] *Rongfeng Guan, Xiaoxue Wang, Qian Sun.* J. Nanomaterials. Nanomaterials for Solar Energy Harvesting and Storage, Volume 2015, doi.org/10.1155/2015/579489/

[7] *Seigo Ito, Toshihiro Ryo.* Advances in Materials Science and Engineering. Volume 2012, Article ID 136092, 6 pages. doi:10.1155/2012/136092

[8] *Min Li, Yafen Xia, Yong Luo, Yaqiong Zhong, Jiaolin Cui.* J. Physical Chemistry Chemical Physics, v. 22, Issue 13, 2020, pp. 6993-7003

[9] *N.M. Gasanly.* Optik, Volume 127, Issue 12, 2016, Pages 5148-5151.

[10] *B.K. Ridley.* Quantum Processes in Semiconductors. U.S.A. Oxford University Press, 1993, p. 394.

THERMODYNAMIC FUNCTIONS OF ELECTRONS IN KANE TYPE SEMICONDUCTOR TUBE

A.M. BABANLI[1], B.G. IBRAGIMOV[2,3]

[1]*Department of Physics, Süleyman Demirel University, 32260 Isparta, Turkey*
[2] *Ministry of Science and Education, İnstitute of Physics, Baku, Azerbaijan, AZ 1143,*
H. Javid ave., 131
[3]*French- Azerbaijan University, Baku Azerbaijan*
e-mail address: arifbabanli@sdu.edu.tr

The energy spectrum and heat capacity of Kane electrons on the surface of a nanotube in a longitudinal magnetic field are investigated for degenerate electron gas. It was shown, that at low temperatures, the specific heat of electrons on the surface of the tube varies linearly with temperature.

Low-dimensional systems based on semiconductors have been the object of great interest for many years since there are numerous applications in technology based on these systems. The interest of scientists in semiconducting heterostructures, quantum dots [1,2], and nanosystems on curved surfaces increases.

In the paper, Ermolaev [3] thermodynamic functions have been calculated in the effective mass approximation for degenerate and nondegenerate electron gases on the semiconductor cylindrical nanotube surface in a longitudinal magnetic field.

An analytical expression for the energy of a relativistic electron on a nanotube in an external magnetic field was obtained using the Dirac equation in [4]. Using this energy spectrum, the thermodynamic functions of the nanotube at low and high temperatures were calculated. The thermodynamic and magnetic properties of electrons in superlattices on the surface of a nanotube in a longitudinal magnetic field are investigated in Ref. [5].

A standard nanotube model is used: a sheet of 2D electron gas rolled into a cylinder with metallic conductivity. The peculiarity of this model system is that it allows us to obtain an exact solution to the problem of the electron energy spectrum.

In this work, using a three-band Kane's model including the conduction band, light, and spin–orbital hole bands, the energy spectrum of carriers on the surface of a tube in a vertical magnetic field is derived.

In the three-band Kane's Hamiltonian, the valence and conduction bands interaction is taken into account via the only matrix element P (the so-called Kane's parameter). The system of Kane equations including the nondispersional heavy hole bands has the form [6]:

$$-EC_1 - \frac{Pk_-}{\sqrt{2}}C_3 + \sqrt{\frac{2}{3}}Pk_zC_4 + \frac{Pk_+}{\sqrt{6}}C_5 + \frac{Pk_z}{\sqrt{3}}C_7 + \frac{Pk_+}{\sqrt{3}}C_8 = 0 \tag{1}$$

$$-EC_2 - \frac{Pk_-}{\sqrt{6}}C_4 + \sqrt{\frac{2}{3}}Pk_zC_5 + \frac{Pk_+}{\sqrt{2}}C_6 + \frac{Pk_-}{\sqrt{3}}C_7 - \frac{Pk_z}{\sqrt{3}}C_8 = 0 \tag{2}$$

$$-\frac{Pk_+}{\sqrt{2}}C_1 - (E + E_g)C_3 = 0 \tag{3}$$

$$\sqrt{\frac{2}{3}}Pk_zC_1 - \frac{Pk_+}{\sqrt{6}}C_2 - (E + E_g)C_4 = 0 \tag{4}$$

$$\sqrt{\frac{2}{3}}Pk_zC_2 + \frac{Pk_-}{\sqrt{6}}C_1 - (E + E_g)C_5 = 0 \tag{5}$$

$$\frac{Pk_-}{\sqrt{2}}C_2 - (E + E_g)C_6 = 0 \tag{6}$$

$$\frac{Pk_z}{\sqrt{3}}C_1 + \frac{Pk_+}{\sqrt{3}}C_2 - (\Delta + E + E_g)C_7 = 0 \tag{7}$$

$$\frac{Pk_-}{\sqrt{3}}C_1 - \frac{Pk_z}{\sqrt{3}}C_2 - (\Delta + E + E_g)C_8 = 0 \tag{8}$$

Here P is the Kane parameter, E_g the band gap energy, Δ the value of spin–orbital splitting, and $k_{\pm} = k_x \pm ik_y$, C_i are envelope functions. The zero of energy is chosen at the bottom of the conduction band. For a uniform magnetic field H directed along the z-axis, the vector potential may be chosen in the form

$$\vec{A} = \left(-\frac{H.y}{2}, \frac{H.x}{2}, 0 \right) \tag{9}$$

$k_{\pm}$ have the forms

$$k_{\pm} \to k_{\pm} \pm i\frac{1}{2}\lambda_H r_{\pm} \tag{10}$$

where

$$r_{\pm} = x \pm iy, \quad \lambda_H = \frac{eH}{\hbar c} \tag{11}$$

Substituting expressions (3)–(8) into formulas (1) and (2), and using relations (9), (10) we obtain two coupled equations for the spin-up and the spin-down conduction band:

$$\left(\begin{array}{c} -E + \frac{P^2}{3}\left(\frac{2}{E+E_g} + \frac{1}{E+E_g+\Delta} \right)\left(-\nabla^2 + \lambda_H L_z + \frac{1}{4}\lambda_H^2 \rho^2 \right) \\ \pm \frac{P^2 \lambda_H}{3}\left(\frac{1}{E+E_g} - \frac{1}{E+E_g+\Delta} \right) \end{array} \right) C_{1,2} = 0 \tag{12}$$

where L_z z component of angular momentum operator and $\rho^2 = x^2 + y^2$, ∇^2 is the three-dimensional Laplacian. In cylindrical coordinates the eigenfunctions

$$C_{1,2} = A \exp\left(im\varphi + ik_z z \right) Q_{1,2} \tag{13}$$

where A is a normalization factor and the energy spectrum of carriers in a Kane-type semiconductor tube is satisfies

$$\frac{3}{P^2}\frac{E(E+E_g)(E+E_g+\Delta)}{3E+3E_g+2\Delta} = \frac{\left(m+\frac{1}{2}\lambda_H \rho^2 \right)^2}{\rho^2} + k_z^2 \pm \lambda_H \frac{\Delta}{3E_1+3E_g+2\Delta} \tag{14}$$

Here the magnetic quantum number m has the values $m = 0, \pm 1, \pm 2, \ldots$. For the strong spin-orbit approximation, $\Delta \to \infty$ Eq. (14) transforms as

$$E(E+E_g) = \frac{2P^2}{3}\left(\frac{1}{\rho^2}\left(m+\frac{1}{2}\lambda_H \rho^2 \right)^2 + k_z^2 \pm \lambda_H \frac{1}{2} \right) \tag{15}$$

The matrix element P^2 is expressed in terms of the effective mass of electrons m_n as

$$\frac{2P^2}{3E_g} = \frac{\hbar^2}{2m_n} \tag{16}$$

If we choose zero of energy in the middle of the energy gap $E \to E - \dfrac{E_g}{2}$ we find the energy levels of electrons (sign +) and light holes

$$E = \pm\sqrt{\frac{E_g^2}{4} + \frac{\hbar^2 E_g}{2m_n \rho^2}\left[(m+f)^2 \pm f + k_z^2 \rho^2 \right]} \tag{17}$$

15

The energy spectrum is a sequence of one-dimensional subbands with the number m.
where

$$f = \frac{\rho^2 \lambda_H}{2} = \frac{\Phi}{\Phi_0} \tag{18}$$

$\Phi = \pi \rho^2 H$ is the magnetic flux and $\Phi_0 = \dfrac{2\pi\hbar}{e}$ is the flux quantum. As seen from Eq. (17) the energy

spectrum of electrons in the surface tube is not additive. Under the radical is the square of the energy of the longitudinal motion of the Kane electron in the tube and the square of the energy of a charged rotator in a magnetic field.

For the energy spectrum (17) the density of states of a Kane-type nanotube can be written as

$$g(E) = \sum_{lk_z\sigma} \delta(E - E_{lk_z\sigma}) = \frac{LE}{\pi} \sqrt{\frac{2m_n}{\hbar^2 E_g}} \sum_{m\sigma} \frac{\Theta(E - u_{m\sigma})}{\sqrt{E^2 - u_{m\sigma}^2}} \tag{19}$$

where $\Theta(x)$ is the Heaviside function and

$$u_{m\sigma} = \sqrt{\frac{\hbar^2 E_g}{2m_n \rho^2}\left[(m+f)^2 + \sigma f\right] + \frac{E_g^2}{4}} ; \sigma = \pm 1 \tag{20}$$

As seen from Eq.(19) the density of states has a singularity, when energy coincides with $u_{m\sigma}$ it is convergent to infinity. Using the density of states (19) we can calculate the number of electrons N, their energy E, chemical potential, and heat capacity C. We consider degenerate electron gas at the surface in Kane type of semiconductor nanotube. The total number of electrons can be found as follows.

$$N = \sum_{mk_z\sigma} f(E) = \frac{L}{2\pi} \sum_{mk_z\sigma} \int_{-\infty}^{\infty} f(E) \frac{dk_z}{dE} dE = \int_{u_{m\sigma}}^{\infty} f(E) g(E) dE \tag{21}$$

where f(E) Fermi-Dirac distribution functions. The total energy of electrons

$$U = \int_0^\infty E g(E) f(E) dE \tag{22}$$

At zero temperature the number of electrons

$$N = \int_u^\mu g(E) dE \tag{23}$$

After integration we get

$$N = \frac{L}{\pi} \sqrt{\frac{2m_n}{\hbar^2 E_g}} \sum_{m\sigma} \sqrt{\mu^2 - u_{m\sigma}^2} \tag{24}$$

the energy of electrons in Kane type nanotube according to (22)

$$U = \frac{L}{\pi} \sqrt{\frac{2m_n}{\hbar^2 E_g}} \sum_{m\sigma} \left(\frac{1}{2} \mu \sqrt{\mu^2 - u_{m\sigma}^2} + u_{m\sigma}^2 Arcch \frac{\mu}{u_{m\sigma}} \right) \tag{25}$$

By using the Sommerfeld method [7] we find temperature correction of the energy of electrons in nanotube

$$\delta E(\mathrm{T}) \approx \frac{\pi^2 k_B^2 T^2}{6} \left(\mu g'(\mu) + g(\mu) \right) \tag{26}$$

Expressing μ in (26) using the zero-order approximation $\mu = \mu_0$. İf μ lies far from the borders of the subzones the specific heat of electrons at the surface nanotube is

16

$$C = \frac{2\pi^2 k_B^2 T}{3} g(\mu) \qquad (27)$$

From these formulas, it is seen that with the change in the magnetic field, every time the u_m coincides with the Fermi boundary the heat capacity experiences a sharp jump, i.e. has a peculiarity.

CONCLUSIONS

The thermodynamic functions of degenerate electrons on the surface of Kane-type semiconductor nanotubes in a longitudinal quantizing magnetic field are calculated. It has been observed that the specific heat and density of states oscillates as the magnetic field varies.

---

[1] *R. Saito, G. Dresselhaus, M.S. Dresselhaus.* Physical Properties of Carbon Nanotubes, Imperial College Press, London, 1998.

[2] *P.N. Dyachkov.* Electronic Properties and Application of Nanotubes, Binom. Laboratory of Knowledge, Moscow, 2012.

[3] *A.M. Ermolaev and G.I. Rashba.* J. Phys. Condens. Matter 20, 175212 (2008)

[4] *N.V. Gleizer, A.M. Ermolaev and G.I. Rashba.* International Journal of Modern Physics B Vol. 33, № 22 (2019) 1950253

[5] *A.M. Babanlı.* Low Temperature Physics, Fizika Nizkikh Temperatur, 2023, Vol. 49, № 2, pp. 220–224

[6] *F.M. Gashimzade, A.M. Babayev, S. Çakmak, Ş. Çakmaktepe.* Physica- E 23, Issues 1–2, June 2004, Pages 177-182

[7] *B.M. Askerov, S. Figarova.* Thermodynamic, Gibbs Method and Statistical Physics of Electron. Berlin: Springer Verlag, 2010, 374 p.

VISCOSITY OF LIQUIDS IN A NONSTATIONARY TEMPERATURE FIELD

A.N. JAFAROVA, A.A. HADIEVA

Department of Physics, Azerbaijan State Oil and Industry University, Azerbaijan
E-mail: aymin@mail.ru

In this paper, we've got the law of variation of dynamic viscosity in the nonstationary regime, i.e. directly in the process of performing technological operations on the basis of input and output information. A formula that establishes a relationship between the viscosity in the nonstationary and stationary regime is also obtained.

INTRODUCTION

A large number of theoretical and experimental studies have been devoted to the investigation of fundamental thermophysical parameters of liquids [1-3]. Interest in researching the thermophysical properties of liquids is due to the fact that by controlling these properties with the help of various physical fields it is possible to increase the efficiency of technological processes.

Taking into account that the thermophysical parameters of the liquids are very sensitive to the conditions for their determination, in order to increase the accuracy of the measurements, the laboratory experimental setups have become more and more complicated all the time, and it was still impossible to completely simulate the real conditions.

It should be noted that in nature all real processes are nonstationary and therefore methods for determining the thermophysical parameters of liquids based on stationarity of processes have limits of applicability. Thermophysical parameters of liquids, determined on the basis of stationarity of processes, are constant and do not change with time. And in the case of non-stationary processes, the thermophysical properties of liquids vary with time, i.e. the relaxation of the parameters takes place, and the relaxation time of these parameters is different. In this connection, in order to determine thermophysical parameters in the nonstationary regime, a method is proposed that would make it possible to establish a relationship between stationary and nonstationary properties of liquids.

THEORETICAL STUDIES AND DISCUSSIONS

One of the important thermophysical parameters of liquids, as is known, is the dynamic viscosity. In non-stationary mode, the pressure drop, as well as the fluid flow rate varies with time. Then it is obvious that the formula for determining the viscosity coefficient derived for the case of constant pressure and flow of liquids will differ from the formula for the variable pressure and the flow rate of the liquid.

The laminar stationary motion of a viscous liquid in a capillary tube is described by the equation:

$$\eta\left(\frac{d^2\upsilon}{dr^2} + \frac{1}{r}\frac{d\upsilon}{dr}\right) + \frac{\Delta p}{\ell} = 0 \qquad (1)$$

The amount of fluid flowing through the cross section of the pipe per unit time, i.e. flow rate is determined by the formula:

$$Q = \int_0^R 2\pi r \upsilon(r) dr = const \qquad (2)$$

From the solution of equation (1) under the conditions $\upsilon(R) = 0$, $\upsilon(0) \neq \infty$ and using Eq. (2) to determine the viscosity coefficient, the formula

$$\eta = \frac{\pi R^4 \Delta p_\infty}{8\ell Q_\infty} \qquad (3)$$

Where the index «∞» corresponds to the stationary motion, i.e. $t \to \infty$. Formula (3) determines the viscosity in a stationary state. In the nonstationary regime, the viscosity $\eta(t)$ as well as the stationary one is theoretically determined by solving the inverse problem for the Navier-Stokes equation. From the solution of this equation, one can find the relationship between viscosity in the nonstationary $\eta(t)$ and stationary regime η. The nonstationary laminar motion of a viscous incompressible fluid in a capillary tube is described by a differential equation:

$$\rho \frac{\partial \upsilon}{\partial t} = \eta(t)\left(\frac{\partial^2 \upsilon}{\partial r^2} + \frac{\partial \upsilon}{\partial r}\right) + \frac{\Delta p(t)}{\ell} \qquad (4)$$

To solve the differential equation (4), the averaging method [4] is applied. Following [4], we introduce the function $\varphi(t)$

$$\varphi(t) = \frac{1}{R}\int_0^R \frac{\partial \upsilon}{\partial t}(r,t)dr \ . \tag{5}$$

Taking into account (5), the differential equation (4) is written as follows

$$\frac{1}{r}\frac{d}{dr}\left(r\frac{d\upsilon}{dr}\right) = \frac{\varphi(t)}{\upsilon(t)} - \frac{\Delta p(t)}{\rho\ell\upsilon(t)} \tag{6}$$

The solution of this equation under the conditions noted above has the form:

$$\upsilon(r,t) = \frac{1}{4}\left(r^2 - R^2\right)\left[\frac{\varphi(t)}{\upsilon(t)} - \frac{\Delta p(t)}{\rho\ell\upsilon(t)}\right] \tag{7}$$

The flow rate through the pipe cross-section is determined by the formula

$$Q(t) = \frac{\pi R^4}{8\upsilon(t)}\left[-\varphi(t) + \frac{\Delta p(t)}{\rho\ell}\right] \tag{8}$$

To determine $\varphi(t)$ let's put the value $\upsilon(r,t)$ from (7) into (5), then we have

$$\varphi(t) = -\frac{R^2}{6}\left[\frac{\varphi(t)}{\upsilon(t)} - \frac{\Delta p(t)}{\rho\ell\upsilon(t)}\right]' \ . \tag{9}$$

Performing differentiation in (9), we obtain the following equation for determining $\varphi(t)$

$$\frac{d\varphi}{dt} + \left(\frac{6\upsilon}{R^2} - \frac{\upsilon'}{\upsilon}\right)\varphi = \frac{\Delta}{\rho\ell} - \frac{\Delta p}{\rho\ell\upsilon} \tag{10}$$

The solution of this equation is expressed by the formula

$$\varphi(t) = e^{-\Phi(t)}\int_0^t\left(\frac{\Delta p'}{\rho\ell} - \frac{\Delta p\upsilon'}{\rho\ell\upsilon}\right)e^{\Phi(t)}dt \ , \tag{11}$$

whereas $\Phi(t) = \int_0^t(\frac{6\upsilon}{R^2} - \frac{\upsilon'}{\upsilon})dt.$ from joint solution (8) and(11) we get an equation for determining the viscosity coefficient for the nonstationary motion of a viscous liquid in a capillary tube:

$$\frac{8\upsilon(t)Q(t)}{\pi R^4} - \frac{\Delta p(t)}{\rho\ell} = e^{-\Phi(t)}\int_0^t(\frac{\Delta p'}{\rho\ell} - \frac{\Delta p\upsilon''}{\rho\ell\upsilon})\,e^{\Phi(t)}\,dt \tag{12}$$

Solving equation (12) we obtain the following formula for determining the non-stationary viscosity

$$\eta(t) = \frac{\pi R^4\Delta p(t)}{8Q(t)\ell} - \frac{\rho R^2}{6Q(t)}Q' \tag{13}$$

Obviously, if $\Delta p = const \ \ Q = const$ then formula (13) coincides with formula (3) for the stationary case. From a comparison of (3) and (13) we have

$$\frac{\eta(t)}{\eta_\infty} = \frac{Q_\infty}{Q(t)}\left[\frac{\Delta p(t)}{\Delta p_\infty} - \frac{4\rho\ell}{3\pi R^2\Delta\rho_\infty}\frac{dQ}{dt}\right] \tag{14}$$

Formula (14) establishes the relationship between stationary and non-stationary viscosities of liquids

CONCLUSION

Application of formula (14) does not require the creation of a special laboratory installation. To use formula (14), it is sufficient to know the flow rate and the pressure drop over time in a certain section of a pipe of length *l*. The proposed formula (13) makes it possible to determine the law of viscosity change with time in the region of the nonstationary field and can be used as the basis for creating an automated system for continuous measurement of thermophysical parameters of liquids.

_____

[1] *V.G. Pridanov, V.I. Khonichev.* 2012. On the flow of non-Newtonian fluid. Journal of Technical Physics. 82, p.11-14.

[2] *G.T. Hasanov, A.N. Mammadova.* 2005. Nonstationary method for determining the heat capacity of liquids", Proceedings of ANAS, series of physicotechnical and astronomical sciences, Volume 25, №2, pp. 167-170.

[3] *Kh.G. Hasanov.* 2009. Hydrodynamic studies of the interaction of acoustic and laser radiation with a liquid", Baku, Publishing house «Stake», p. 336.

[4] *N.A. Slezkin.* 1955. Dynamics of a viscous incompressible fluid", Moscow, "Fizmatgiz", p. 519.

EFFECT OF HEAT TREATMENT ON POLYPROPYLENE AND
METAL OXIDE (PP+ZrO₂) NANOCOMPOSITES

H.S. IBRAGIMOVA¹, R.L. MAMMADOVA²

¹ Institute of Physics, Ministry of Science and Education of Azerbaijan, Baku, Azerbaijan
²Sumgayit State University
hicran90@rambler.ru

The presented research work specifies the charge state before and after heat treatment of nanocomposites composed of isotactic polypropylene and metal oxide nanoadditive ZrO_2. It has been established that PP+3% ZrO_2 nanocomposites have the ability to retain a greater charge. The parameters of the electret state of a nanocomposite of a given composition at different temperature values have been obtained by the TSD method. It is concluded that the maxima in the region of low and high temperatures are due to charges accumulated in crystalline and amorphous phases and boundaries of polymer nanocomposites. The results of the conducted studies correlate with the results of the SEM.

INTRODUCTION

Polymers are widely used in modern science and technology as electret materials. Examples include radiation transducers, electroacoustic devices, small electret microphones, etc. Polymer electrets are commonly used in mechanical, electrical, acoustic transducers, storage devices, electric motors, generators as elements, friction zones, filters and membranes, anti-corrosion structures and medicine [1, 2]. The main advantage of these devices is the high internal resistance and the lack of an additional power supply. This feature ensures that the size and weight of the device will be small. For further development of such a promising field, it is necessary to obtain new electret materials with a high charge density and the ability to store this charge. For this reason, one of the main goals of modern condensed matter physics is to obtain polymers capable of holding more electret charges. It has been established that when polymers are modified with various substances, including metal oxides, high-density and stably charge-retaining electrets are obtained [3,4]. Modifications can cause a change in the supramolecular structure, provided that the chemical composition is maintained. Thus, in the case of these modifications, oxides of elements are formed in the polymer in the form of nanogroups, and the electret state increases significantly. In the presented research work, the electret state and its parameters obtained after heat treatment using isotactic polypropylene and the metal oxide nanoadditive ZrO_2 as a matrix have been determined.

EXPERIMENTAL METHODOLOGY

When obtaining the nanocomposites under study, first the required amount of isotactic polypropylene (Dema Import and Export Co. Ltd., China) in the form of granules 5 mm in size is weighed with an accuracy of 10^{-4} and dissolved in toluene up to the melting temperature of the polymer (≈175°C). Then, to ensure uniform distribution of the nanoadditive inside the matrix, after its melting, ZrO_2 metal oxide nanoparticles (Sigma-Aldrich, USA) 20-25 nm in size with a monoclinic structure in an amount of 1-15%, stabilized by YtO_3, are added to a completely transparent liquid. After cooling, nanocomposites are obtained by hot pressing under a pressure of 15 MPa for 3 minutes. In the fast cooling mode at a rate of 20-35 °C/sec, the nanocomposites with the foil are placed in an ice-water mixture. The thickness of the samples is 50-70 μm. The change in charge state after heat treatment at various temperatures was determined by the method of thermally stimulated depolarization (TSD). TSD currents were determined at a rate of 4 °C/min in the temperature range of 50-230°C. The activation energy of the particles was calculated by the Garlick-Gibson method using formula

$$\frac{d \ln I(T)}{d(1/kT)} \approx -W \quad (1)$$

based on the slope of the tangents drawn to the TSD currents.

RESULTS AND DISCUSSION

Figure 1 shows TSD curves for PP and PP+ZrO₂ nanocomposite depending on the percentage of nanoadditive. Analysis of the curves shows that they consist of two regions of maximum – low-temperature (20-40°C) and high-temperature (120-150°C). That is, on these curves, along with the peaks corresponding to the PP, other peaks are also observed. According to the results of comparative analysis of TSD spectra, it was found that depolarization maxima appearing in the spectra arise both in the polymer itself and in the layers of PP+%ZrO₂ nanocomposite as a result of relaxation of charges stabilized at the interfacial boundary at characteristic temperatures. The peaks formed in the low temperature region can be attributed to the currents generated by charges released due to heating from defects in the nanocomposite during fabrication. They can be formed as a result of the movement of linked molecular chains in the amorphous phase and free rotation between the lamellae. The maxima in the high temperature region are due to currents created by charges accumulated in

the phase between the polymer and the nanoadditive. The increase in the electret properties of polymers with the addition of ZrO_2 can be explained by the formation of new structural elements that can act as new traps. Moreover, when nanoparticles are added to a polymer, they can serve as crystal nucleation agents or cause crystal defects. As it is seen from the figure, the TSD currents increase up to 3% of the amount of nanoadditive, but at subsequent percentage amounts a decrease in these currents is observed. This is due to the aggregation of the nanoadditive in a given percentage amount.
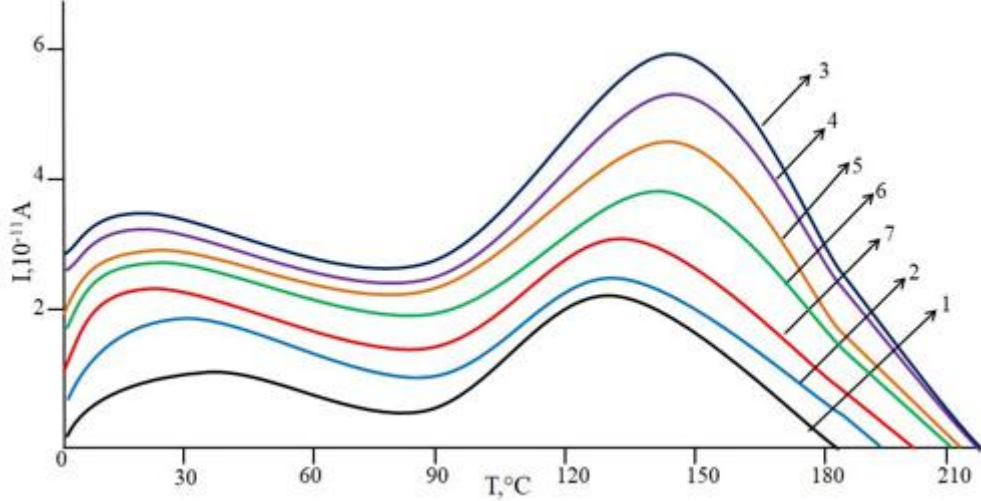

Fig. 1. TSD spectra before heat treatment depending on the percentage of PP and nanoadditive 1 - PP, 2 - PP+10%ZrO₂, 3 - PP+15%ZrO₂, 4 - PP+5%ZrO₂, 5 -PP+1%ZrO₂, 6 - PP+3%ZrO₂, 7 - PP+15%ZrO₂

Let's note that we used formula (2) to calculate the maximum charge

$$Q = \frac{1}{\beta} \int_{T_1}^{T_2} I(T)dT \qquad (2)$$

Here β is the linear heating rate of nanocomposites, T_1 and T_2 are the lower and upper temperature limits of the presence of charges, respectively.

Considering the above, it can be determined that the electret state can be changed by adding a certain percentage of nanoadditive to the PP, and also the parameters characterizing this state can be clarified. However, from the studies carried out it is clear that the relaxation of electret charges weakens when up to 3-10% of a nanoadditive is added to the matrix. When adding 15% nanoadditive, the electret state and the parameters characterizing this state decrease. This is explained by the fact that with a small amount of nanoadditive it acts as a nucleus inside the matrix, and with an increase in the percentage, it acts as a filler [5]. If we examine the table, we can see that the charges accumulated in the surface traps increase up to 3% of the nanoadditive. If we observe the TSD spectra, we will notice that the maxima are obtained between 30-60 °C and 120-150 °C. If we compare the spectral regions of 30-60°C, we will observe that the maxima shift towards lower temperatures and the intensity of the current generated by the TSD tends to decrease. This change can be explained by an increase in the degree of crystallinity depending on the percentage of nanoadditive. The maxima formed in high-temperature regions may be due to space charges generated in the polymer and thermal activation of charge carriers located at the boundary of the polymer nanocomposite.

Figure 2 represents the TSD curves obtained by heating the PP+3%ZrO₂ nanocomposite. To obtain an electret, these samples must be heated to different temperatures and for this reason, the nanocomposite is heated to 60, 100 and 140°C for 2 hours. From the nature of the above curves, it is evident that the heat treatment temperature affects the thermal stability of the nanocomposites. It is clear from the experiments that the electret parameters of thermoelectrets obtained only by heating are less stable. The generated TSD current is due to the self-charges of the polymer and matrix leaving their places under the influence of heat. When the samples are heated, the amount of charge released from the traps begins to change. As the temperature rises, charges begin to release even deep traps, and relax, accelerating in their fields. The frequency of charges released from traps is determined by Boltzmann's law:

$$\omega_t = \omega_0 \exp(-E_k /kT_m) \qquad (3)$$

$$W \approx 25kT_m \qquad (4)$$

where ω_0 is the frequency factor, E_k is the kinetic energy of charges released from traps, k is the Bolsmann constant, and T_m is the maximum temperature in the TSD curves (3). As it can be seen from the formula with increasing temperature, the release frequency from the traps increases exponentially, and the capture time decreases accordingly. On the other hand, according to formula

(4), an increase in temperature leads to an increase in the kinetic energy of charges releasing the traps. The effect of temperature is associated with an increase in the intensity of thermal movement of groups, segments and other kinetic units, which are the main factors influencing the electret state. The presence of maxima in the high temperature region can be explained by an increase in the specific conductivity of the nanocomposite.

Table 1.

Electret parameters of PP and PP+%ZrO₂ nanocomposites depending on the amount of nanoadditive

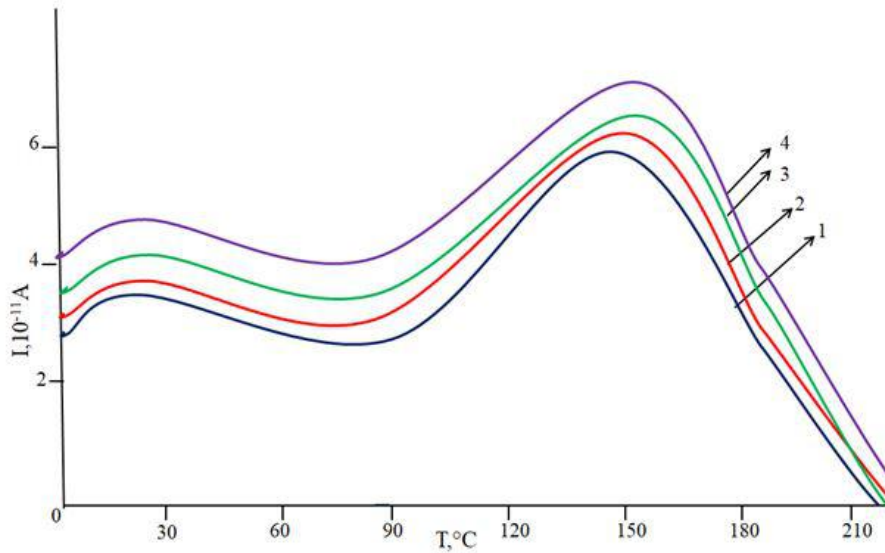| Nanoadditive %	q, (10^{-6} C/m²)		Q(nC)		E(eV)		Temperature (°C)	
	I max	II max	I max	II max	I max	II max	I max	II max
0	1,18	1,87	9,42	13,68	0,024	0,068	43	130
1	1,26	18,5	9,68	14,45	0,026	0,075	32	135
3	2,07	2,97	9,89	15,78	0,029	0,083	29	138
5	2,00	2,43	8,45	14,95	0,023	0,079	27	141
10	1,08	2,95	7,45	13,45	0,089	0,061	20	143
15	1,16	2,02	8,39	13,76	0,099	0,084	17	147

Fig. 2. TSD curves of PP+3%ZrO₂ nanocomposites subjected to heat treatment at different temperatures.

Table 2.

Parameters calculated from the TSD curves of PP+3%ZrO₂ nanocomposites after heating at different temperatures

Heat treatment	q, (10^{-6} C/m²)		Q(nC)		E(eV)		Temperature (°C)	
	I max	II max	I max	II max	I max	II max	I max	II max
T=293K	2,07	2,97	9,89	15,78	0,029	0,063	25	135
T=333K	1,84	4,07	9,98	15,96	0,034	0,088	23	153
T=373K	1,98	4,2	10,5	16,3	0,039	0,9	20	155
T=413K	2,04	4,8	14,4	18,1	0,045	0,16	18	160

Table 2 summarizes the parameters calculated from the TSD curves of PP+3%ZrO$_2$ nanocomposites after heating at various temperatures. In the region of relatively low temperatures (30-60°C), a slight increase in the depolarization current intensity is observed. Relaxation of the accumulated charge occurs preferentially in those temperature regions where relaxation transitions are formed. This shows that the electrical and molecular relaxations in polymers are coupled. The presented table shows that these parameters have a smaller value only in the case of polymer and at low temperature. However, an increase in temperature is accompanied by an increase in the activation energies of charges released from traps. But it was determined that if the electret lifetime is 35 minutes at a temperature of 100 °C, then this time is reduced to 16 minutes at a temperature of 140 °C [6]. When heating without applying an external field, we slow down the polarization process so that the charges displaced relative to each other relax in the internal field of the electret. Thus, the studies carried out show that very small area electret states are observed in the nanocomposite due to the effect of temperature [7]. Indeed, the temperature we applied can only induce oscillations of the CH chains of the polymer and the nanocomposite.

If we examine the SEM images of the investigated nanocomposites, we can see agglomerations formed on the surface after two-hour heat treatment, which is a manifestation of defect formation in the nanocomposite. In general, if crystallite melting and structure rearrangement occur during the first hours of heat treatment, then the accumulation of particles of a certain structure is noticed during the subsequent intensification of the heat treatment effect. Figure 3 shows the SEM images before and after heat treatment.
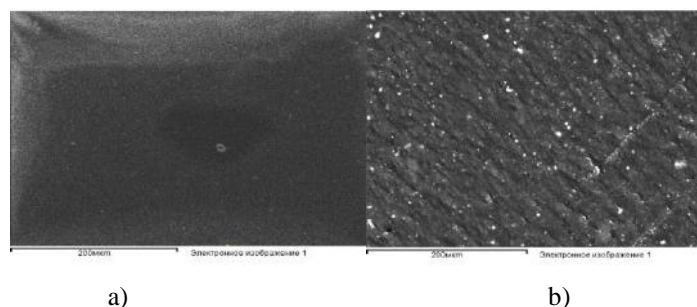

a)   b)

Fig. 3. SEM images of PP+3%ZrO$_2$ nanocomposite before (a) and after 2-hour heat treatment (b).

Thus, the conducted studies allow us to conclude that by introducing nanometaloxides into polymers it is possible to regulate the stability of the electret states of these substances, and also that the maxima on the TSD curves after temperature treatment are achieved due to the charges possessed by the polymer and nanocomposite, which are accelerated and leave the material as a result of thermal effects.

[1] *M.F. Galikhanov.* 2020 Change of structure and properties of polymer corona electrets due to fine filler. AIP Conference Proceedings**,** 2308, 030015-2-7. DOI:10.1063/5.0034680

[2] *Maria Raimo.* Growth of spherulites: foundation of the DSC analysis of solidification ChemTexts (2015) 1:13 DOI 10.1007/s40828-015-0013-1

[3] *D.G. Izha, S.V. Polunin, L.F. Klabukova, M.V. Goroshkov, A.P. Krasnov.* Study of Tribological Properties of Filled Polyphenylenesulfide Advances in chemistry and chemical technology. VXXXIV. 2020. № 7

[4] *Z. Guo, Y. Patil, A. Shinohara, K. Nagura, M. Yoshida, T. Nakanishi.* 2022. Organic molecular and polymeric electrets toward soft electronics Molecular Systems Design and Engineering, 7, 537-552.
DOI: 10.1039/DIME00180A

[5] *H.S. Ibrahimova**,** H.A. Shirinova, R.M. Rzayev, K.E. Rahimova, E.M. Mustafayeva.* Change of Thermophysical Parameters of Polypropylene – Metal Oxide nanoco(polypropylene +ZrO$_2$) After Electric Field Influence. Journal Polymers and Polymer Composites 2022, 30, 1-6 DOI:10.1177/09673911221104484.

[6] *E.M. Gojaev, A.M. Magerramov, Sh.A. Zeynalov, S.S. Osmanova, E.A. Allakhyarov.* Coronoelectrets based on composites of high density polyethylene with semiconductor filler TlGaSe$_2$ Electronic Processing of Materials Volume 46 (2010), Number 6, pp. 91-96.

[7] *A.M. Magerramov, R.L. Mammadova, I.M. Ismailov, H.V. Bagirbekov.* Dielectric properties of polypropylene/nanoclay nanocomposites of Na+-montmorillonite type in heating-cooling mode Journal of Technical Physics, 2017, Vol. 87, Iss. 9.

FIRST-PRINCIPLES STUDY OF ELECTRONIC AND MAGNETIC PROPERTIES OF DEFECTED ZnSe

V.N. JAFAROVA, V.K. SARIJANOVA, M.A. MUSAEV

Azerbaijan State Oil and Industry University, 20 Azadlig ave., AZ-1010, Baku, Azerbaijan
E-mail: vusale.cafarova@asoiu.edu.az

Electronic and magnetic properties of defected ZnSe 32- and 96-atom supercell systems were investigated from the first-principles study. We obtained that the presence of one, two, and three Zn vacancies defects lead to the magnetization of ZnSe with ~2 μ_B total magnetic moment and main contribution to magnetization of systems come from host Se atoms. The ferromagnetic alignment in the Zn vacany defected ZnSe supercell systems show semiconducting nature.

Keywords: ZnSe, Zn vacancy, electronic, magnetic properties.
PACS: 61.43.Bn; 71.20.-b; 61.72.-y; 75.50.Pp; 68.55.Ln

1. INTRODUCTION

Transition-metal doped ZnSe supercell systems have revealed its potential for technical application. ZnSe is ideally appropriate for the fabrication of photodetectors, CO_2 laser focusing lenses, sensors, solar cells, and other photovoltaic applications [1]. This material can be applied for the production of optoelectronic devices such as light emitters and detectors [2-5]. The Zn(Fe)Se has been applied to the laser gain medium in mid-IR laser [6].

DMSs based on II-VI group compounds have been attracting great interest as promising materials for new spin electronic devices, because these compounds show ferromagnetic (FM) phase, who's Curie temperature, depends on the carrier concentration [7]. For industrial applications of DMSs room temperature, ferromagnetism is strongly required. Doping of TMs in nonmagnetic wurtzite ZnSe semiconductor is very impotant to make this material multifunctional. These materials have attracted a lot of attention as materials for spintronic applications because of their half-metallic ferromagnetic (HMFM) behaviors.

Investigations show that numerous research works devoted investigation of electronic and magnetic properties of defected zinc-blende ZnSe systems. Rai *et al* [8] studied 5 Zn vacancies in the monolayer hexagonal ZnSe 18-atom supercell modeled by 3×3×1 transferred based on the DFT. They reported that the Zn vacancy makes the FM state of ZnSe.

2. CALCULATION METHOD

The calculations were carried out for the ZnSe systems with 32 and 96 atoms by the DFT method within Local Spin Density Approximation (LSDA) implemented Atomistix ToolKit code within incorporated Mulliken population analysis. The interactions between the electrons and ions, and exchange-correlation were described by the Fritz-Haber-Institute ion pseudopotentials and the Perdew Zunger (PZ) functional, respectively. The Kohn-Sham wave functions expanded in a linear combination of atomic orbitals with a kinetic energy cutoff of 75 Ha. When cal-culating structural and electronic properties for pure compound, the primitive cell of ZnSe wurtzite containing 2 Zn and 2 Se atoms and the atomic positions are optimized until the force and stress on each atom converges to less than 0.001 eV/Å and 0.001 eV/Å³, respectively. The supercells containing dopant atoms and vacancies were optimized with force and stress tolerances of 0.01 eV/Å and 0.01 eV/Å³, respectively. The reciprocal space integration was performed with 5×5×5 (for supercells) and 7×7×7 (for bulk structure) Monkhorst-Pack *k*-point sampling and a standard electron temperature of 300 *K*.

The 12 electrons for Zn [Ar] $+3d^{10}4s^2$ and 6 electrons for Se [Ar] $+4s^24p^4$ are treated as the valence electrons. The Hubbard *U* corrections took 4.5 eV for Zn 4*d*- and 3.5 eV for Se 4*p*-states.

RESULTS AND DISCUSSION
3.5 ZnSe supercell with Zn vacancy

ZnSe crystallizes in the wurtzite structure, a hexagonal analog of zinc blende lattice, with a space group P6₃mc with two formula units per unit cell. In this structure, each Zn atom is tetrahedrally coordinated with four other Se atoms and the atomic positions for zinc are (0, 0, 0) and (1/3, 2/3, 0.5), for selenium are (0, 0, 0.3408) and (1/3, 2/3, 0.8408) [38].

The first-principles computed Zn-Se and Zn-Zn (Se-Se) distances have been found equal to 2.39 and 3.9 Å, respectively. We get a structure with an average Zn-Se bond length of 2.39 Å and this value is in agreement with the reported results by Chen *et al* (theor.: 2.376 Å) [9] and Park *et al* (exp.: 2.20 Å) [10].

The magnetic properties of 32- and 96-atom supercells ZnSe wurtzite structure with vacancy defects at Zn sites (Figure 1). In this figure, the Zn vacancy-defect position is encircled. The studied structure is formed by the admixture of ionic and covalent bonds. One vacancy defect at the Zn site in systems creates the dangling of three Zn-Se covalent bonds and this fact will give three extra acceptors which will induce the spin magnetic moment at the nearest 4 Se atoms dangling bonding of Zn. Rai *et al* [8] and Chan *et al* [11] have reported a similar fact.
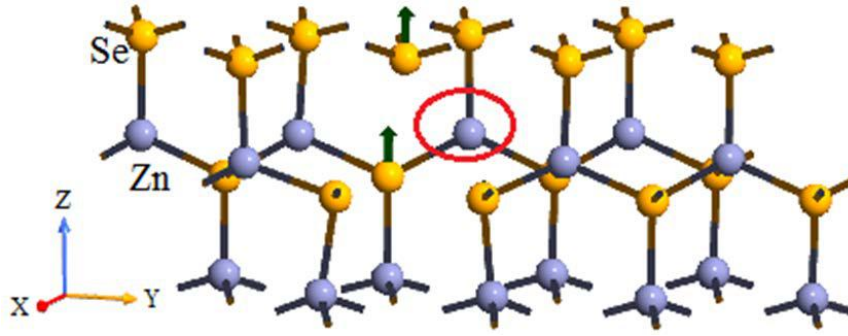
Fig. 1. The 32-atom ZnSe supercell structure and magnetization with one Zn vacancy-defected (Zn-gray, Se-yellow).
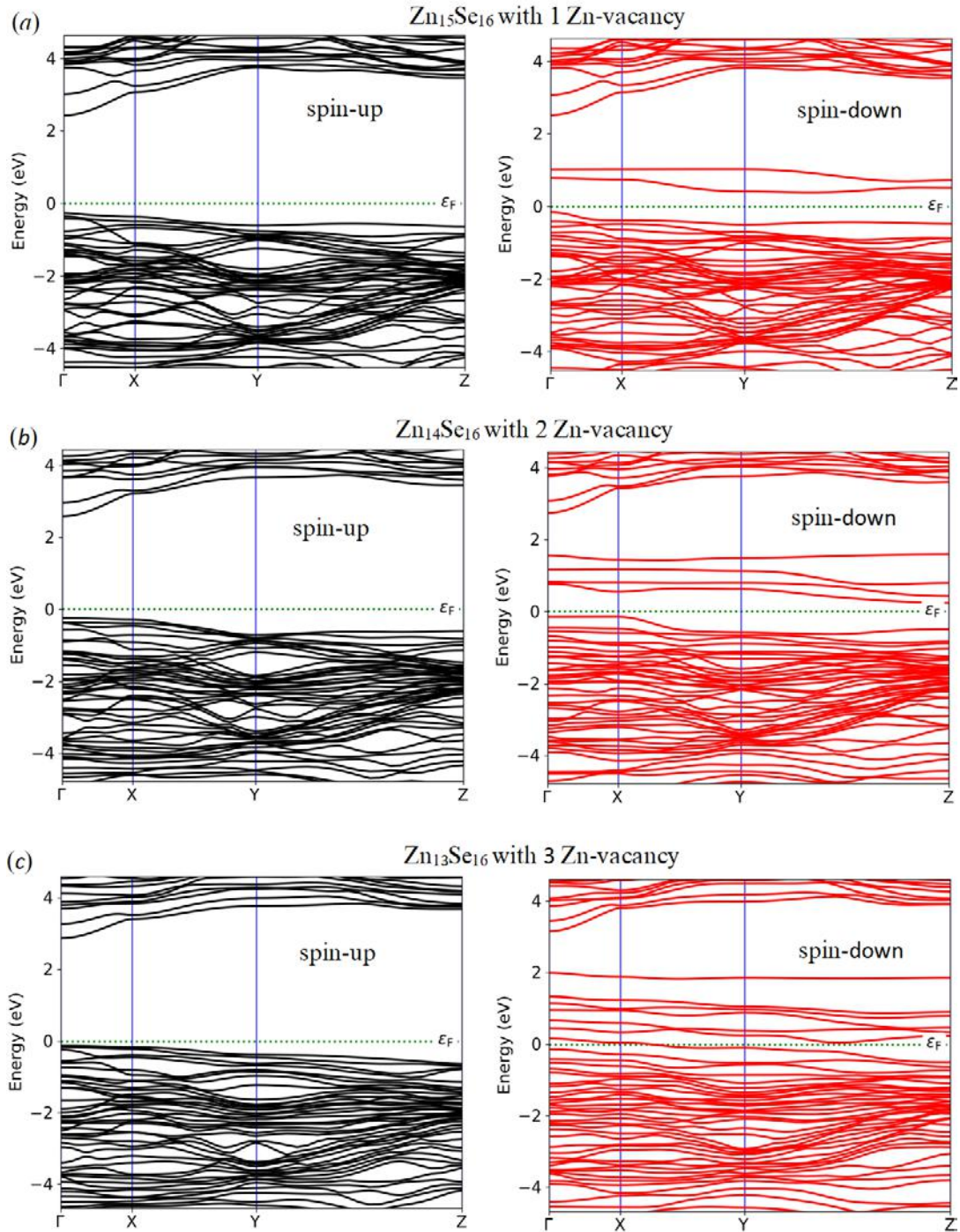

Fig. 2. The DFT-LSDA+U calculated electron band structures of $Zn_{15}Se_{16}$ (a), $Zn_{14}Se_{16}$ (b), and $Zn_{13}Se_{16}$ (c) systems with vacancy-defects at Zn sites: black-spin-up; red-spin-down states.

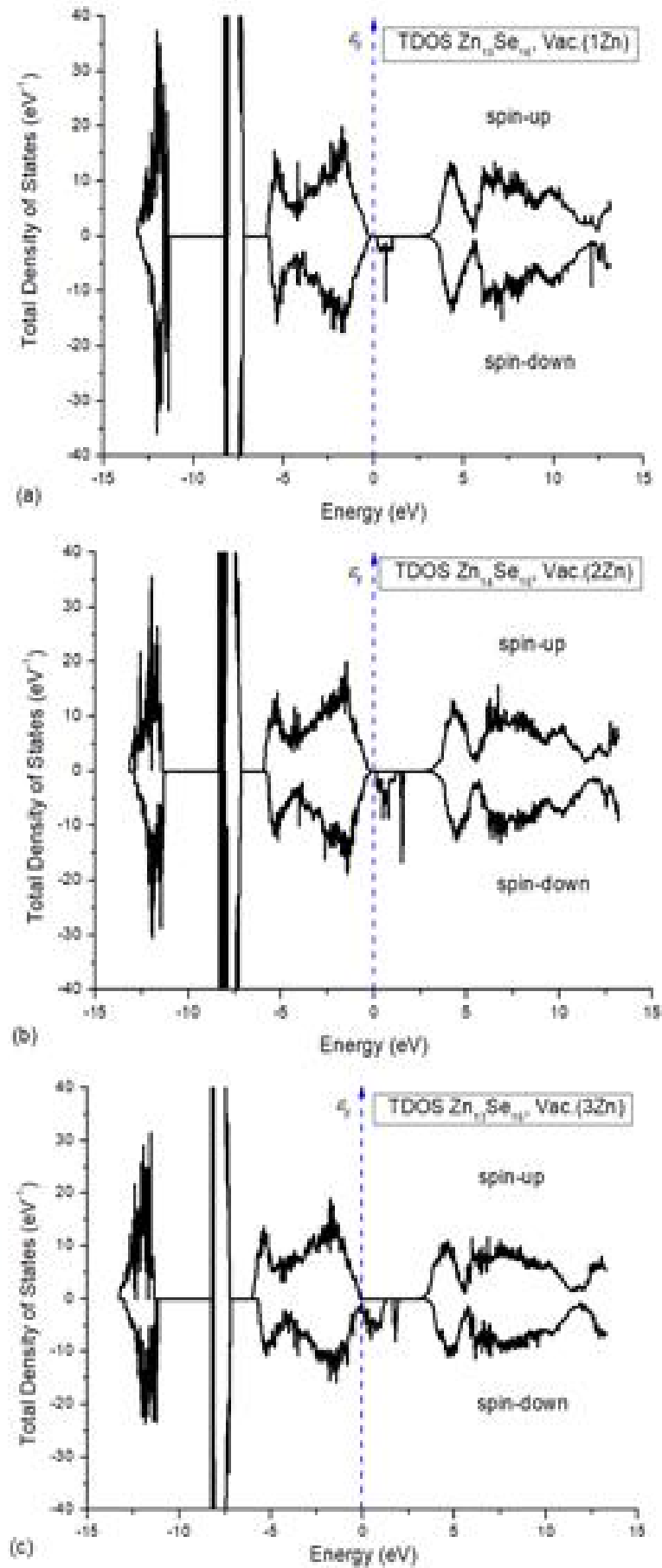*Fig. 3.* The DFT-LSDA+U calculated the TDOS of $Zn_{15}Se_{16}$ (a), $Zn_{14}Se_{16}$ (b), and $Zn_{13}Se_{16}$ (c) systems with vacancy-defects at Zn sites.

To obtain accurate band gap value, we first have been calculated the band structure of for ZnSe bulk structure and obtained the band gap of 2.7 eV [12, 13]. This value is very close with experimental results. The first-principles calculated band gap and magnetic moment results for vacancy-defected ZnSe systems for spin-up and spin-down states are presented in Table 1. Zn vacancy case increases the spin-up band gap,

but decreases the spin-down band gap of $Zn_{1-x}Se$ systems, dependent on the number of vacancies. In this case, due to the presence of one (or two and or three) zinc vacancy-defect the total magnetic moment of the system is about ~2 μ_B (main contributions to the magnetization including 2.288 μ_B (2.34 μ_B) from 16 Se (or 48 Se) and -0.289 μ_B (-0.352 μ_B) from 15 Zn (or 47 Zn) atoms).

Table 1.

The band gap and magnetic moment results of vacancy-defected ZnSe for spin-up and spin-down states.

Supercell	Band gap, eV		μ_B per Vac.(Zn)
	Spin-up	Spin-down	
$Zn_{15}Se_{16}$	2.68	1.5	1.999
$Zn_{14}Se_{16}$	2.8	1.18	1.999
$Zn_{13}Se_{16}$	3.0	1.16	2.01
$Zn_{47}Se_{48}$	2.70	1.5	1.988

The values of total magnetic moments for ZnSe 32-atom supercells with one (1.99 μ_B; 1.83 μ_B), two ((1.99; 1.97 μ_B), and three Zn vacancy-defects (2.01 μ_B; 1.72 μ_B) calculated from Mulliken Population analyses well agree with the known theoretical results reported by Rai et al [8]. The positive contributions to magnetization from Se (2.288 μ_B) and smaller negative contributions from Zn atoms (-0.289 μ_B) of supercell.

Figures 2 and 3 show band structures and TDOS for Zn vacancy defected $Zn_{1-x}Se$ (x=1, 2, 3) systems. As seen in figure 8, the TDOS of major- and minor-spin states are not symmetric, because Zn vacancy-defects in ZnSe systems lead to the ferromagnetic spin ordering. DFT calculations revealed that present Zn vacancy cases increase the spin-up band gap, but decrease the spin-down band gap of $Zn_{1-x}Se$ systems, dependent on the number of vacancies.

DFT-LSDA+U calculations revealed that the availability of one Zn defect into the ZnSe supercell is the most effective for strengthening the magnetization. Thus, the shift of the moment of the system due to one Zn vacancy side is (1.6 ÷ 1.9) μ_B depending on the chosen location of the defect.

CONCLUSION

In summary, the spin-polarized electronic properties of ZnSe with Zn vacancy are studied by DFT within the LSDA+U method. The investigations performed for 32- and 96-atom ZnSe supercell systems show that Zn vacancy lead to a ferromagnetic spin ordering. The existence of defects in the structure affects the magnetization of the supercell with ~2 μ_B total magnetic moment. Our calculation revealed that in the Zn vacancy case, increases the spin-up band gap, but decreases the spin-down band gap of $Zn_{1-x}Se$ systems, dependent on the number of vacancies. The Zn vacancy is the most efficient for enhancing supercell magnetization.

––––––––––––––––––––––––––––––––––––––

[1] *G.F. Neumark, R.M. Park, J.M. Depuydt*, Physics Today, 1994, v.47, p.26.

[2] *B.I. Adetunji, P.O. Adebamboand G. A. Adebayo*, J. Alloys Compd.*, 2012, v.513, p.294.

[3] *M. A. Haase, J. Qiu, J.M. De Puydt and H. Cheng*, Appl. Phys. Lett., 1991, v.59, p.1271.

[4] *D.B. Eason, et al.,* Appl. Phys. Lett., 1995, v.66, p.115.

[5] *A.F. Gochuyeva, Kh.Kh. Hashimov, I. Y. Bayramov,* Chalcogenide Letters, 2023, v.20, p.285.

[6] *S.B. Mirov*, *et al.*, OSA Proc. Adv. Solid-State Lasers, AM4A., 2014, v.6, p.16.

[7] *G.A. Medvedkin, et al.*, Jpn. J. Appl. Phys., 2000, v.39, p. L949.

[8] *D.P. Rai, et al.*, Vacuum, 2020, v.182, p.109597.

[9] *X.L. Chen, et al.*, RSC Adv., 2015, v.5, p.106227.

[10] *H. Park, H. Chung and W. Kim*, Mater. Lett., 2013, v.99, p.172.

[11] *J.A. Chan, L. Stephan, A. Zunger*, Phys. Rev. Lett.*, 2009, v.103, p.016404.

[12] *V.N. Jafarova*, Intern. J. Modern Phys. B, 2022, v.36, p.2250156.

[13] *V.N. Jafarova, H.S. Orudzhev*, Sol. State Commun., 2021, v.325, p.114166.

STUDY OF SOL-GEL PHASE TRANSITION IN THE AGAROSE-WATER SYSTEM BY ELECTRICAL CONDUCTIVITY

E.A. MASIMOV, A.R. IMAMALIYEV, A.H. ASADOVA

Baku State University, Azerbaijan
Email:aynurasadova19@gmail.com

In the present work the electrical conductivity method was used to study the sol-gel phase transition in the agarose-water system. The 0.1% agarose-water system is used for this purpose; The temperature dependence of the conductivity of 0,1%, 0.3% and 1% solutions and as well as the influence of hydrophobic (isoamyl alcohol) and hydrophilic (Na salt of tartaric acid) additives on this dependence were studied.It was shown that the hydrophilic additive makes the gel more stronger and shifts the gelation (Tg) and melting (Te) temperatures up. The hydrophobic additive (hydrophobic isoamyl alcohol) on the contrary weakens the gel and shifts the gelation (Tg) and melting (Te) temperatures downward.

INTRODUCTION

Polymers (and their alloys) can be divided into two types according to their electrical conductivity: neutral and charged polymers [1,2]. Examples of neutral polymers among the natural polymers are gelatin and agarose. Gellan, carrageenan, etc. biopolymers related to the charged biopolymers [3]. The solution of these biopolymers in water becomes a gel above a certain concentration (x_g) and below a certain temperature (T_g), that is, it retains its shape (loses fluidity) under small mechanical influences. This feature of the gel is associated with the presence of a three-dimensional spatial network, in the core of which water is immobilized, and opens the way to numerous applications [4].

The study of electrical conductivity in polymer gels carries some information about their structure [5]. In addition, since electrical conductivity around phase transitions undergoes a significant change, the measurement of electrical conductivity makes it possible to determine the points of phase transitions with some accuracy. Conductivity studies in such systems play an important role when choosing a model to study electrical properties of the brain or the effect of electric fields on the central nervous system [6].

It was mentioned above that agarose, a typical representative of natural polysaccharides, is an uncharged (neutral) polymer and possesses many useful properties: bioabrasiveness, biocompatibility, strong thermally reversible gel-forming ability, etc. Due to these properties, agarose is now successfully used for drug delivery to the target organ [7,8] and in tissue engineering [9]. When applied, it is necessary to adapt the physical (mechanical, thermal, electrical, etc.) of the agarose gel to the required values, which is achieved by changing the agarose concentration and adding additives of different nature to the gel. In fact, this is done by modifying the gel structure. It was mentioned above that the study of electrical conductivity plays a role in the study of gel structure. The present work studied the dependence of agarose gel conductivity on agarose concentration, temperature, and the influence of hydrophilic and hydrophobic additives on these dependencies.

EXPERIMENT

Agarose is the main component of red algae agar, and its monomer (agarobiose) has the following chemical structure [9]:
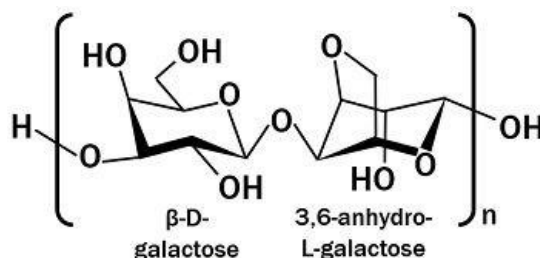
The agarose gel was prepared as follows [10]. Agarose powder was weighed on ADAM PW 124 (USA) (accuracy 0.1 mg) and added to bidistilled water. After 1 day of storage (swelling process), the mixture is heated to 95°C. The samples are poured into a glass bath containing platinum electrodes in the form of a solution (sol) and cooled to room temperature. The area of the platinum electrodes is 1 cm2 and the distance between them is 0.2 cm. Isoamyl alcohol $((CH_3)_2CH(CH_2)_2OH)$ was used as a hydrophobic additive in an amount of 1% by weight, and Na-salt of tartaric acid $(C_4H_4O_6Na_2*2H_2O)$ was used as a

hydrophilic additive. The electrical properties of the agarose gel were measured on an IET 1920 LCR meter (USA) at a frequency of 2 kHz. The measuring voltage (test signal) applied to the sample was 0.5 V. In an AC circuit, when the liquid dielectric is poured into a bath with platinum electrodes, it can be considered as a capacitor of capacity C and a resistor of resistance R connected in parallel. In this case the electrical conductivity is calculated by the following formula:

$$\sigma = \frac{d}{RS}$$

Here S is the area of the electrodes, and d is the distance between the electrodes.

Temperature was measured using a chromel-alumel thermocouple. The temperature generated at the thermocouple outlet was measured with an EHQ B7-21 microvoltmeter (Russia). When the solution is in gel form, measurements are taken after holding for at least one hour at each temperature because agarose gel takes a long time to reach thermodynamic equilibrium. Therefore, a GL-100 thermostat (China) was used to ensure temperature stability during measurements.

RESULTS AND THEIR EXPLANATION

The results of measurements are presented in graphs 1-4. Figure 1 shows the temperature dependences of the electrical conductivity of the agarose gel at different concentrations in both the heating and cooling modes. Since the 0.1% agarose solution did not form a gel, the dependence showed no hysteresis. The critical concentration of agarose for gel formation is about 0.15% [11]. Although the agarose hydrogel is a thermally reversible gel, there is a strong thermal hysteresis in its physical properties. That is, when heated and cooled, the values of the physical quantities characterizing the gel (radiation coefficient, flux voltage, electric voltage, etc.) do not overlap at the same temperature. Confirmation of this can be seen in 0.3% and 1% solutions (curves 2 and 3 in Fig. 1). These curves can be characterized as follows. When the gel is heated from room temperature, its electrical conductivity increases. At a certain temperature (60-80°C) this increase occurs with a small jump. Obviously, this is due to the disintegration of the spatial mesh of the gel. This temperature is called the gel melting temperature or the temperature of the gel-sol phase transition (T_m). When the resulting solution (sol) cools from 90 to 95 ˚C, the conductivity decreases, but the curve goes over the top because the bulk network is not restored. Recovery of the spatial network occurs at very low temperatures (30-40 ˚C), which again is accompanied by a weak jump in the decrease of conductivity. This jump is associated with the sol-gel phase transition, and the corresponding temperature is called the transition temperature (Tg). Thus, according to curves 2 and 3, the gel formation temperature is $T_g = 35°C$ for a 0.3% weak agarose gel and $T_g = 40°C$ for a 1% strong gel. The melting temperature of the 0.3% gel T=65°C and the 1% gel T=75°C.

Figure 2 shows the dependence of the conductivity of agarose solution on the concentration of agarose at 25 ˚C. As can be seen, the conductivity decreases with increasing concentration. The main reason for this is that the mobility of ions decreases with increasing polymer concentration as a result of increasing solution viscosity. Another reason is the decrease in ion mobility as a result of the compression of the spatial network nuclei as the concentration increases, when the solution is in the form of a gel.
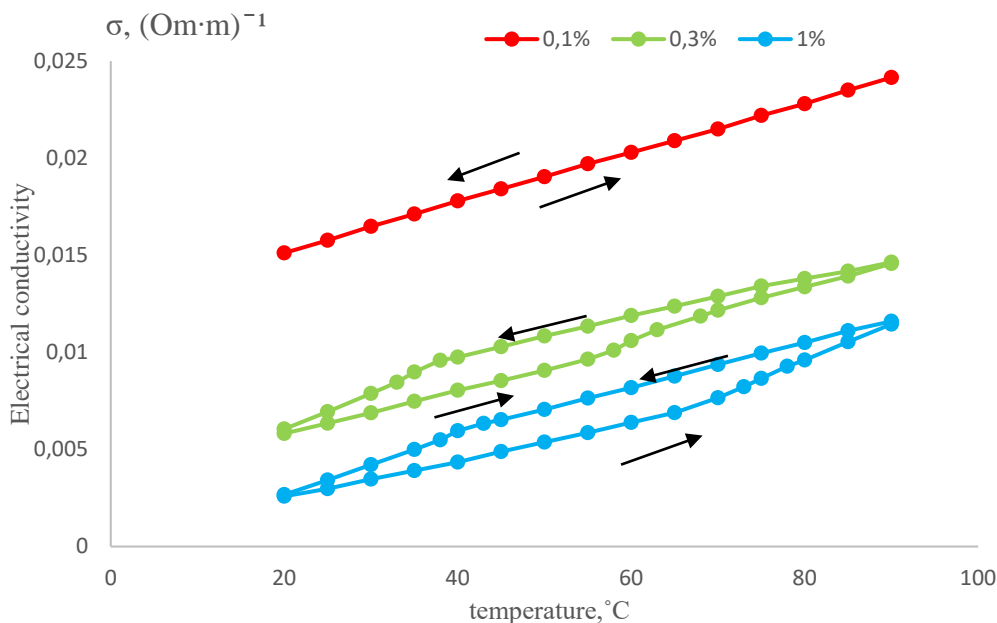

Fig.1. The dependence of electrical conductivity on temperature for different concentrations of agarose-water systems.
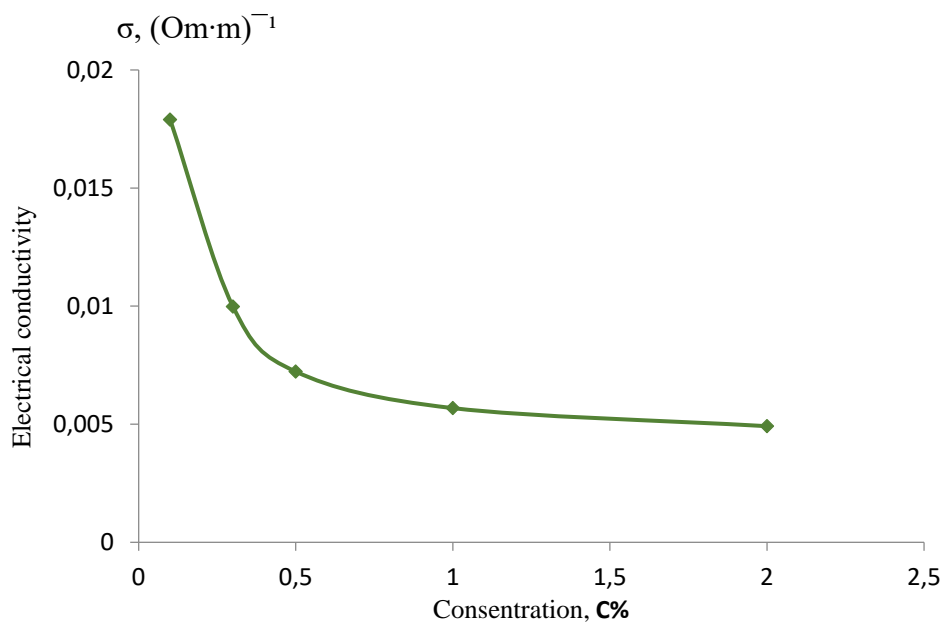
Fig.2. The dependence of agarose gel conductivity on the consentration of agarose-water systems.
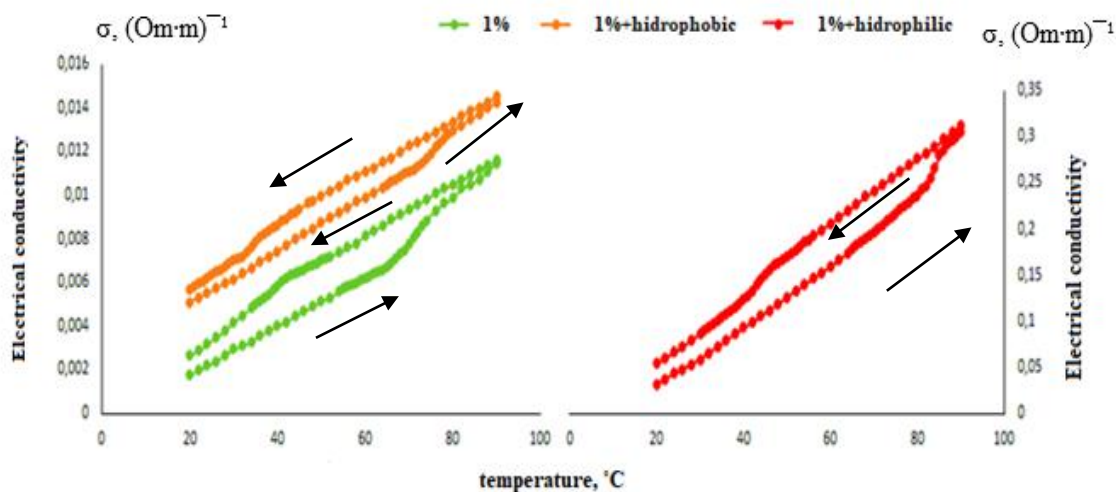

Fig. 3. The effect of hydrophobic (isoamyl alcohol) and hydrophilic (Na salt oftartaric acid) additives on the agarose gel on electrical conductivity.

Fig. 3 shows temperature dependences of electrical conductivity of 1% agarose gel and 1% gel with hydrophobic and hydrophilic additives. In both cases the gel conductivity increases. Hydrophobic additive increases the conductivity by 2-3 times, and hydrophilic additive increases the conductivity by at least one compilation.

In addition, hydrophobic and hydrophilic additives shift the gel melting and gelation temperatures in opposite directions. For example, when 1% isoamyl alcohol (hydrophobic) is added to 1% agarose gel, the gelation temperature decreases from 40 ˚C to 36 ˚C and melting temperature decreases from 75 ˚C to 73 ˚C, so the hydrophobic additive weakens the gel. Adding 1% sodium salt of tartaric acid to 1% agarose gel, the gelation temperature increases from 40 ˚C to 45 ˚C, and the melting temperature of the gel from 75 ˚C to 82 ˚C, so the hydrophilic additive makes the gel more stronger.

The results for all graphs-the temperature dependence of agarose concentration and the temperature dependence curve of electrical conductivity at each concentration when the hydrophobic and hydrophilic additives are added-are summarized in Table 1. It should be noted that T_g and T_m determined by the coductometric method and this results differ by 1-2 ˚C with the results of the optical method.

Table 1.

C %	Agarose gel, t_g (°C)	Agarose gel, t_m (°C)	Agarose gel + hydrophilic additive t_g (°C)	Agarose gel + hydrophilic additive t_m (°C)	Agarose gel + hydrophobic additive t_g (°C)	Agarose gel + hydrophobic additive t_m (°C)
0.1	–	–	30	45	-	-
0.3	35	58	40	70	31	61
0,5	36	60	39	66	33	58
1	40	75	45	82	36	73
2	41	88	46	90	38	86

Electrical conductivity in the agarose-water system occurred due to the dissociated H^+ and OH^- ions of water and some ionic additives (charged radicals) due to incomplete purification of agarose biopolymer.

It should be noted that the amount of these ions is very less, that is why the given porsion of water to the conductivity is more greater.

_____

[1] *A.K. Mishra.* Conducting Polymers: Concepts and Applications, Journal of Atomic, Molecular, Condensate & Nano Physics, 2018, v.5, №2, 159-193.

[2] *G. Kaur, R. Adhikari, P. Cass, M. Bown, P. Gunatillake.* Electrically conductive polymers and composites for biomedical applications, *RSC Adv.*, 2015, 5, 37553–37567.

[3] *U.W. Gedde, M.S. Hedenqvist.* Fundamental Polymer Science, Springer, 2018, 501 p

[4] *V.K. Takur, M.K. Takur, S.I. Voicu.* Polymer Gels: Perspectives and Applications, Springer, 2018, 419 p.

[5] *R. Singh, P.K. Singh, V. Singh, B. Bhattacharya.* Agarose biopolymer electrolytes: ion conduction mechanism and dielectric studies, *Cellulose Chem. Technol.*, 2017, v. 51, (9-10), 949-955(2017).

[6] *R. Pomfret, K. Sillay, G. Miranpuri.* Investigation of the electrical properties of agarose gel: characterization of concentration using Nyquist plot phase angle and the implications of a more comprehensive *in vitro* model of the brain,

Annals of Neurosciences, v.20, №3, 2013, 99-107.

[7] *M. Chelu, M.A. Musuc.* Polymer Gels: Classification and Recent Developments in Biomedical Applications, *Gels,* 2023, v.9, 161-187.

[8] *A. Ullah, M.H. Othman, F. Javed, Z. Ahmad, H. Akil.* Classification, processing and application of hydrogels: A review, Materials Science and Engineering, C 57 (2015) 414–433.

[9] *A. Taghizadeh, M. Taghizadeh, P. Zarrintaj, J.D. Ramsey, S. Habibzadeh, F. Seidi, M.R. Saeb, M. Mozafari, M.A. Salati, J. Khazai, A.M. Tahmuri, A. Samadi,* Agarose-Based Biomaterials: Opportunities and Challenges in Cartilage Tissue Engineering, *Polymers* 2020, *12*, 1150-1165.

[10] *E.A. Masimov, A.R. Imamaliyev and A.H. Asadova,* Spectrophotometric investigation of gel formationin water solution of agar, Modern Physics Letters B, 2050147 (7 pages).

[11] *M. Tako, S. Nakamura.* Gelation mechanism of agarose, Carbohydrate Research, 1988, 180 (2), 277-284.

IR ANALYSIS OF COPPER DOPED Ni-Zn NANOFERRITES

I.F. YUSIBOVA[1], Sh.N. ALIYEVA[2]

[1] *Institute of Physics, Ministry of Science and Education of Azerbaijan Republic, Az-11143 Baku, Azerbaijan*
[2]*Departament of Physics, Azerbaijan State Oil and Industry University, Az-1010 Baku, Azerbaijan*
yusibova78@mail.ru

Nanocrystalline ferrites $Ni_{0.4}Zn_{0.6-x}Cu_xFe_2O_4$ (x=0-0.6) were synthesized by a high-temperature method based on metal oxides. The IR measurements showed the presence of noticeable bands caused by vibrations of metal ions and which are a feature of the formation of the spinel ferrite phase. A shift in the IR bands due to doping concentration was observed.

Keywords : nanoferrit, IR analysis, sublattice

INTRODUCTION

Ferrites are materials of great practical, technological and theoretical importance. High magnetic permeability, mechanical strength, electrical resistivity, high thermodynamic and chemical stability, heat resistance and corrosion resistance make these materials important [1]. The demand for this type of magnetic materials is increasing with the development of technology. Ferrite materials are used in almost every element of electrical devices manufactured today [4, 5, 6]. The properties of ferrites depend on several factors: composition, manufacturing method, temperature, doping with various cations, grain size and location, etc. Ferrites, which make up the main group of ferromagnets, have the general formula $MeFe_2O_4$, where Me is a divalent metal ion, such as Me - Mn^{2+}, Fe^{2+}, Co^{2+}, Ni^{2+}, Cu^{2+}, Zn^{2+}, Mg^{2+} and Cd^{2+}The spinel lattice is a face-centered cubic lattice with oxygen anions (O^{2-}) at the nodes. Two types of sublattices are formed between the position: The Me^{2+} ion is located in the tetrahedral A-sublattice, and the Fe^{3+} cation is located in the octahedral B-sublattice. The spinel lattice consists of 32 oxygen ions and 24 metal ions. According to their structure, spinels are divided into 3 groups: normal, reverse and mixed. In transformed spinels, the Me^{2+} ion is in sublattice B, and the Fe^{3+} ion is in sublattices A and B. In mixed spinels, Me^{2+} and Fe^{3+} ions are in both sublattices[4, 8,9]. Scientific papers have published about Ni-Zn ferrites, mainly electrical, magnetic, optical, etc., which are of interest from the point of view of the practical application of these ferrites. more attention was paid to studying its characteristics. However, the dependence of these characteristics on their composition and structure has not been sufficiently studied. It is from this point of view that the study of ferrite materials in this area is relevant. In the presented work, the replacement of the Zn ion by the Cu ion in Ni-Zn ferrite was investigated. These elements differ in their atomic mass, ionic radius [7, 10].

PREPARATION OF SAMPLES

The properties of ferrite materials, which have a wide range of applications, differ significantly from each other depending on their chemical composition, raw materials used, processing and synthesis methods. Information about the technology of ferrite synthesis was published in [1]. It is known that for each ferrite, taking into account the required properties, a suitable technological method must be developed. There are many methods for synthesizing ferrite materials: oxide mixing, thermal decomposition, co-precipitation method, etc. The most common synthesis method for obtaining pure ferrite material of good quality is the high-temperature "ceramic" method. Ferrites with a cubic structure are formed as a result of a diffusion reaction in mixtures of metal oxides in the solid phase at high temperatures. The chemical activity of the components, particle sizes and homogeneity largely influence the completeness of the diffusion reaction between mixtures of metal oxides in the solid phase and, as a consequence, the properties of the resulting ferrites. The disadvantage of this method is that the process occurs at high temperatures (above 1200°C), which causes an increase in the size of ferrite particles and a weakening of the magnetic properties. Various methods are used to reduce the synthesis temperature of Ni-Zn ferrites. [1, 2, 3] showed that the addition of Cu ions to Ni-Zn ferrites makes it possible to obtain composites at lower temperatures, but Cu ions reduce the resistivity of the samples, which is unfavorable for their use at high frequencies. Taking into account the above, nanopowders of the general formula $Ni_{0.4}Zn_{0.6-x}Cu_xFe_2O_4$were obtained by high-temperature synthesis. For this purpose, stoichiometric amounts of the corresponding metal oxides ZnO, NiO, CuO, Fe_2O_3 (purity 99% in all cases) were used as raw materials. The process was carried out in several stages. Initially, the corresponding metal oxides were calcined at 900°C for 3 hours and then tempered at 950°C for six hours. The quality of the synthesized ferrite powders was assessed using an XRDD8 ADVANCE X-ray diffractometer (Bruker, Germany) [2, 5, 6].The infrared spectra of $Ni_{0.4}Zn_{0.6-x}Cu_xFe_2O_4$ ferrite powders were studied in a vacuum chamber in the spectral range of 4000-400 cm^{-1} with a standard spectral resolution of 0.5 cm on a Vertex70 infrared Fourier spectrometer (Bruker, Germany) with an Easi DiffTMM attachment for measuring diffuse reflections (PIKETechnologies, USA).

RESULTS AND DISCUSSIONS

Infrared analysis is one of the important methods for studying the formation of the spinel ferrite phase, in addition to X-ray diffraction analysis. In the case of

33

spinel ferrites, the most interesting part of the IR spectra is in the range of 800 – 250 cm^{-1}. According to Waldron and Hafner [11, 12], the bands around 600 cm^{-1} (ν_1) are attributed to stretching vibrations in tetrahedral positions and the bands around 400 cm^{-1} (ν_2) in octahedral positions.

Table 1.
Variation of band position ν_1 and ν_2 (cm^{-1}) for $Ni_{0.4}Zn_{0.6-x}Cu_xFe_2O_4$ (x=0-0.6) nanoparticles

x	$\nu_1(cm^{-1})$	$\nu_2(cm^{-1})$
0.0	563	476
0.12	562	480
0.24	554	475
0.3	570	485
0.36	552	481
0.48	561	471
0.6	587	482

The change in the position of the ν_1 and ν_2 bands of $Ni_{0.4}Zn_{0.6-x}Cu_xFe_2O_4$ is shown in Table 1. The change in the position of the v1 peak for samples with different x indicates that with a change in composition, structural changes occur in the tetrahedral positions. The position of the band and its shape are significantly affected not only by the chemical composition of the sample, but also by a number of uncontrolled parameters, such as synthesis conditions, annealing temperature, etc. A shift of the ν_1 band towards lower wave numbers is observed with increasing x. over the entire composition range. This indicates a weakening of metal-oxygen bonds at tetrahedral sites. Thus, we can conclude that a change in the size of nanoparticles causes a change in the positions of ν_1 and ν_2 of the infrared bands [13].

CONCLUSIONS

Ferrite nanoparticles $Ni_{0.4}Zn_{0.6-x}Cu_xFe_2O_4$ (x=0-0.6) were synthesized by a high-temperature method based on metal oxides. IR spectra is one of the important methods for studying the formation of the spinel ferrite phase. IR analysis showed noticeable bands due to vibrations of metal ions. The positions of the bands were found to be very sensitive to doping conditions. Structural changes were confirmed by a shift in the position of the bands due to Cu doping.

_____

[1] *N.N. Sholtz, K.A. Piskarev.* Ferrites for radio frequencies, Moscow 1966, 131 p.

[2] *M. Usakova, J. Lukac, R. Dosoudil, V. Jancarik, A. Gruskova, E. Usak, J. Slama, J. Subrt.* J. Mater Sci: Mater Electron. 2007,18: p.1183-1189.

[3] *A.S. Padampalle, A.D. Suryawanshi, D.D.Suryawanshi, S.S. Patil and S.K. Gurav.* 2018: Special Issue A2:168-171.

[4] *E.V. Gorter.* УФН, т. LVII, вып. 2, 1955, pp. 279-346

[5] *Sh.N. Aliyeva.* Azerbaijan Journal of Physics, vol. XVII, N 1, Section: Az, March, 2011

[6] *M.F. Huq, D.K. Saha, R. Ahmed and Z.H. Mahmood.* Ni-Cu-Zn Ferrite Research: A Brief Review. J. Sci. Res., 2013, 5(2), 215-233.

[7] *S. Akhter, D.R. Paul, Md.A. Judge, D. Kumar Saha, Al-Mamun Md., A. Parveen.* Materials Sciences and Applications, 2011, 2, 1675-1681.

[8] *S.N. Aliyeva, A.M. Kerimova, R.B. Abdullayev, T.R. Mehdiyev.* Physics of the Solid States 2017, v. 59, ISSUE 3, p. 543-549.

[9] *Sh.N. Aliyev, A.M. Kerimova, R.B. Abdullaev, T.R. Mekhtiev.* ФТТ, т. 59 вып. 3, p. 528-533.

[10] *M. Molaahmadi1, S. Baghshahi1, A. Ghasemi.* J Mater Sci: Mater Electron 27, 2016, p.11447-11456.

[11] *R.D. Waldron.* Phys. Rev., 1955, 99, 1727.

[12] *S.T. Hafner, J.Kristallogr.* 115 (1961) 331.

[13] *T. Suto, K. Haneda, T. Iijima, M. Seki.* J. Appl. Phys. A 50 (1990) 13.

CONTENTS